Hindawi
International Journal of Energy Research
Volume 2024, Article ID 7105454, 29 pages
https://doi.org/10.1155/2024/7105454

Research Article

Active Flow Control of the Magnetohydrodynamic Flow in an Annular Linear Induction Pump by Modifying the Driving Electromagnetic Field

Xiaojie Wang,[1] **Dayong Wang**,[1] **Xing Zhang**,[2] **Di Xia**,[2] **Yun Zhong**,[2] **and Ruijie Zhao**[1,3]

[1]*Research Center of Fluid Machinery Engineering and Technology, Jiangsu University, Zhenjiang 212013, China*
[2]*Shanghai Nuclear Engineering Research & Design Institute Co., Ltd., Shanghai 200233, China*
[3]*Wenling Fluid Machinery Technology Institute of Jiangsu University, Wenling 317500, China*

Correspondence should be addressed to Ruijie Zhao; rjzhao@ujs.edu.cn

Received 20 October 2023; Revised 29 February 2024; Accepted 4 March 2024; Published 28 March 2024

Academic Editor: Ahmad Azmin Mohamad

The strong coupling between fluid and electromagnetic field in the annular linear induction pump (ALIP) can gradually amplify small disturbance in the fluid field into large-scale vortices. The appearance of the vortices seriously affects the efficiency and reliability of the pump. An active flow control method based on the modification of the driving electromagnetic field is proposed to improve the flow stability. A simplified numerical model of the ALIP is established to simulate the three-dimensional flow in the annular flow channel, and the internal electromagnetic field is modified by using the modulated surface current. The influences of the active flow control method on the flow behavior, pressure pulsation, and energy conversion are, respectively, investigated based on the simulation results. The results show that the modulated surface current can accelerate the vortical evolution. The size and strength of the vortices are suppressed in the modified electromagnetic field. The pressure pulsation low frequency at the ALIP's outlet is significantly reduced when the modulated surface current density reaches a certain level. The surges in the processes of energy conversion become more gentle within the control method, and the overall energy efficiency is slightly reduced even at the highest modulated surface current density.

1. Introduction

The electromagnetic (EM) pump is an indispensable equipment for transporting conductive fluids in diverse energy conversion systems, such as liquid metal-cooled nuclear reactors, aerospace, metal casting, and chip heat dissipation [1–3]. Compared with the mechanical pumps, the advantages of the EM pump are of contactless drive, no-moving parts, leakage free, and low vibration and noise [4, 5]. It is quite suitable in the application in which high reliability and long-life service within extremely harsh conditions are required. Among different types of EM pumps, the annular linear induction pump (ALIP) has been receiving more attention due to its inherent facility of large-size application. For example, it has been intensively studied as the coolant pumps for the primary and secondary circuits of the fourth-generation neutron-cooled fast reactor [6–8]. Although the ALIP has a superior performance in terms of stability and safety, the energy efficiency of ALIP is usually lower than the mechanical pumps [9, 10]. More importantly, the conveyed liquid metals in ALIP can suffer from unstable flows, e.g., vortex and reversed flows, at the off-design flow rates, resulting in large pressure pulsation at the pump's outlet [6]. These phenomena will further deteriorate the energy efficiency and reliability of ALIP. Therefore, the prediction and control of the unstable flows in ALIP are the critical issues for maintaining the stable working condition of ALIP.

The early research on this topic comes from Gailitis and Lielausis [11]. They proposed a determination criterion for occurring the unstable flow in ALIP, $R_m \bullet s > 1$, where $\mathrm{Re}_m = \mu\sigma u L$ and s are the magnetic Reynolds number and the velocity slip, respectively, μ is the magnetic permeability of the fluid, σ is the conductivity of the fluid, u is the characteristic velocity of the fluid, and L is the characteristic length. This

criterion shows that the phenomenon of unstable flow is more likely to occur in the ALIP if the flow condition and magnetic field satisfy the proposed condition. Then, Kirillov and Ostapenko [12] experimentally verified the proposed criterion, and it is found that the low frequency pulsations in the flow rate and pressure at the ALIP's outlet are attributed to the inhomogeneous flows in the ALIP. Later on, Araseki et al. [13] further studied the performance of an ALIP prototype under various working conditions, and it is found that the pressure pulsation of double-supply-frequency (DSF, double of the frequency of input current) is mainly due to the cutting effect of the induced magnetic field at both ends of ALIP. Subsequently, Araseki et al. [6] developed a two-dimensional (2D) numerical model of the ALIP to simulate the coupling effect between the fluid and magnetic fields. Although the prediction accuracy of the numerical model is moderate, it is firstly verified in the simulation that the pressure pulsation low frequency is related to the large-scale vortex that occurred in the flow channel at the off-design flow rates.

Besides the experimental studies, the effort has been made in the theoretical analysis of flow instability in ALIP. Werkoff [14] studied the magnetohydrodynamic (MHD) flow instability in liquid metal induction pump based on a linear stability analysis. The effect of the edge waves on the flow stability was firstly considered in the analysis, and it is found that the edge waves can either destabilize or stabilize the MHD flow, depending on the real physical conditions in the studied pump. Kim and Lee [15] derived a linear perturbation equation for the liquid metal in the ALIP's environment under the assumption of small Re_m. The Reynolds number Re and Hartmann number Ha for the flow stability were sought from the condition of existence of a nontrivial solution of the system, Reynolds number $\mathrm{Re} = \rho u L/\mu$ and Hartmann number defined as $\mathrm{Ha} = LB\sqrt{\sigma/\mu}$, where ρ is the density of the fluid and B is the magnetic induction intensity. The results show that the magnetic field can significantly influence the flow stability. Zhao et al. [16] developed an analytic expression for the axial Lorentz force, and the coupling effect between velocity and magnetic field was studied by analyzing the magnitudes of these terms in a nondimensional magnetic induction equation. It is found that the magnetic diffusion is affected by both Re_m and the wave number of the disturbance. This founding successfully explains the physics of the different schemes used to stabilize the flow in ALIP.

Recently, more attention has been paid to develop the more delicate numerical model, which can simulate the ALIP in three dimensional (3D) and full scale. Blanc and Truong [17] performed the numerical simulation of an ALIP based on the finite element method, and the simulation results were compared with the experiment for validation. However, the fluid domain in the pump was assumed as a solid, and thus, the MHD effect was ignored in the fluid domain. Gissinger et al. [18, 19] used the direct numerical simulation method to simulate the liquid metal driven by a travelling magnetic field in a two-dimensional channel (equivalent to the meridian plane of the flow channel of ALIP), and the flow characteristics of the liquid metal under different magnetic field conditions were studied. It is found that there are critical values for Re_m and Ha. When the critical values are exceeded, the flow will stall and the flow stalling is attributed to the weakening of the magnetic diffusion ability in the liquid metal. When Re_m and Ha increase gradually, the fluid state will change from stall to turbulent flow and large-scale vortices appear in the flow channel. Asada et al. [20, 21] have established a 3D numerical model of a large ALIP prototype by using commercial CFD software for fluid dynamics simulation and a self-developed code for EM field simulation. The fluid and magnetic field were coupled, and the behavior of the liquid metal was simulated under different working conditions. The results show that vortices occurred in both the radial and circumferential directions of the pump channel, and the vortical size is increased as the flow rate drops from the nominal rate. Abdullina et al. [22] coupled the EMAG software with the CFX software in the ANSYS platform and performed the simulation on a sliced model of an ALIP prototype. The performance characteristics of the ALIP, e.g., the curve of flow rate versus pressure, were predicted by the simulation. However, the flow instability was not analyzed in the model for that the full-scale flow channel was not simulated in this work and the unstable flow was not observed. Zhao et al. built a 2D coupling numerical model [23] and further a 3D full-scale numerical model to study the internal unstable flows [24]. It is found that the competition between the axial components of the Lorentz force and pressure gradient in the flow dominates the vortical evolution, and the magnetic-fluid coupling can amplify the small disturbance in either the magnetic field or the fluid. After that, Zhao et al. [9] analyzed the evolution of large-scale vortices in terms of energy conversion and found that vortices increase the undesirable induced current and the associated ohmic dissipation, thus reducing the energy conversion efficiency of the pump. From the previous research, it can be seen that the ALIP is prone to occur large-scale unstable flows originating from the small disturbance in the fluid or magnetic field. These large-scale unstable flows can induce the low frequency fluctuations in the flow rate and pressure at the ALIP's outlet, which significantly deteriorates the safety and stability of ALIP system.

From the above literature, the pressure pulsation of DSF is gradually reduced with increasing the pump size. It is also effectively suppressed by designing gradual coiling windings at both ends [25] or the continuous magnetic circuit structure [15]. However, the research on controlling the large-scale vortices in ALIP and the resulting low frequency fluctuations is still scarce. Araseki et al. [26] tried to change the input current phase in order to reduce the disturbance in the EM force. The result shows that the instability of the internal flow is suppressed while the energy efficiency is significantly reduced due to the disorders in the induced magnetic field. Therefore, it is urgent to find a better way to increase the flow stability in ALIP with less sacrifice in the pump efficiency. Chatterjee et al. [27–32] simulated the pipe flow of nanofluid under different magnetic fields and variable thermal conductivities and studied the effects of different flow parameters on velocity distribution, wall shear stress, and flow function.

In this work, a 3D numerical model considering the coupling between the fluid and magnetic field in ALIP is

employed, and the full-scale pump channel is simulated in order to accurately capture the unstable flows evolved in the ALIP. An active flow control strategy is applied to suppress the unstable flows under the off-design conditions. The validation and energy efficiency of the active flow control method are estimated based on the simulation results. The introductions of ALIP and the numerical model are presented in Section 2. The implementation of the active flow control strategy is introduced in Section 3. The influences of the control method on the flow evolution, the pressure pulsation, the processes of energy conversion, and the energy efficiency in the ALIP are also estimated and discussed in Section 3. The conclusions are summarized in the end.

2. Numerical Model of ALIP

2.1. Physical Model. The structural schematic of ALIP is shown in Figure 1. It consisted of the inner and outer stators, a series of coil windings, a flow channel bounded by the inner and outer ducts, and other supporting parts. In the ALIP, a magnetic field travelling along the ALIP's axis can be induced in the outer stator by a three-phase alternative current in the coil windings. The induced magnetic field can penetrate through the flow channel and circulates between the inner and outer stators. In the flow channel, a current is induced along the circumferential direction due to the varying magnetic field. Ideally, both the magnetic field and current are orthogonal, and they are interacted to form the Lorentz force along the third direction, i.e., the axial direction. The conductive flow is pressurized by the Lorentz force since its velocity keeps constantly in the flow channel. Unfortunately, the conductive flow is not always stable. The flow system is complex because the conductive flow is coupled with the magnetic field through the Lorentz force and fluid velocity. On the one hand, the flow movement is governed by the Lorentz force, which is determined by the magnetic field and the induced current in the flow. On the other hand, the induced current is also influenced by the fluid velocity through Ohm's law. From the practical experience, large-scale vortex or reversed flow may occur in the flow channel if a small disturbance is introduced in any of the physical quantities, such as the magnetic field and inlet velocity. Therefore, the full-scale flow channel should be considered in the simulation in order to accurately reproduce the unstable flows.

The finest simulation of the ALIP is intractable in that the complicated geometry of the magnetic excitation part requires a huge amount of elements, along with the narrow air gaps between different parts. In this work, the ALIP was modeled within two simplifications.

(1) The travelling magnetic field created by the stators and coil windings was assumed to be stimulated by a surface current imposed on the outer duct in a harmonic form (Equation (9)), as shown in Figure 2. Therefore, the modeling parts of the inner and outer stators, coil windings, and the ducts were ignored in the model. The full-scale flow channel of the ALIP was retained to accurately simulate the unstable evolution of the liquid metal

(2) The flow channel was extended outside of the EM section in order to consider the "end effect" caused by the interception of the induced magnetic field at both ends of the EM section. A part of the air domain surrounding the flow channel was simulated to facilitate the definition of boundary condition on the outer surface of the non-EM section

The simplified model has significantly reduced the complexity of the model's geometry while the boundary condition of the magnetic field with reasonable accuracy can be defined in the system. The structure and dimensions of the simplified model are shown in Figure 3. Some main parameters and the properties of the simulated liquid metal are presented in Table 1.

2.2. Governing Equations. The numerical simulation of ALIP is composed of two parts: the simulation of the EM field and the simulation of the fluid field. The EM field is solved based on the set of Maxwell's equations. To reduce the computational cost and speed up the coupled calculation, the set of Maxwell's equations based on the $\boldsymbol{A}$ -Φ method is solved, and they are formulated as follows:

$$\nabla \times \left(\frac{1}{\mu}\nabla \times \boldsymbol{A}\right) + \sigma\left(\frac{\partial \boldsymbol{A}}{\partial t} + \nabla\Phi - \boldsymbol{u} \times (\nabla \times \boldsymbol{A})\right) = \boldsymbol{J}_e, \quad (1)$$

$$\nabla \bullet \boldsymbol{A} = 0, \quad (2)$$

where $\boldsymbol{A}$ is the vector magnetic potential (Wb/m) which satisfies $\nabla \times \boldsymbol{A} = \boldsymbol{B}$ and Φ is the electrical potential. At the same time, the Coulomb's gauge $\nabla \bullet \boldsymbol{A} = 0$ is introduced to ensure the uniqueness of the solution for $\boldsymbol{A}$ in the solution domain. $\boldsymbol{J}_e$ is the external current density (A/m^2), σ is the conductivity of liquid sodium (S/m), μ is the permeability of liquid sodium (H/m), and $\boldsymbol{u}$ is the velocity of liquid sodium (m/s).

The governing equations of the fluid field consisted of the incompressible Navier-Stokes (N-S) equations and the continuity equation. The Lorentz force generated by the interaction between the magnetic field and current density is added in the N-S equations as the volume force $\boldsymbol{F}_L$. The fluid turbulence is simulated based on the standard k - ε turbulence model. The governing equations of the fluid field are expressed as follows:

$$\rho\frac{\partial \bar{\boldsymbol{u}}}{\partial t} + \rho(\bar{\boldsymbol{u}} \bullet \nabla)\bar{\boldsymbol{u}} = -\nabla\left(\bar{p} + \frac{2}{3}\rho k\right) + \nabla \bullet \left[\left(\mu_f + \mu_t\right) \cdot \left(\nabla\bar{\boldsymbol{u}} + (\nabla\bar{\boldsymbol{u}})^T\right)\right] + \boldsymbol{F}_L, \quad (3)$$

$$\rho\nabla \bullet \bar{\boldsymbol{u}} = 0, \quad (4)$$

where ρ, μ_f, and μ_t are the density of liquid metal, kinetic viscosity of liquid metal, and turbulent viscosity, respectively, $\bar{\boldsymbol{u}}$ is the mean velocity vector, and $\bar{p}$ is the mean pressure. $\boldsymbol{F}_L = \boldsymbol{J} \times \boldsymbol{B}$ is the Lorentz force, in which $\boldsymbol{J}$ and $\boldsymbol{B}$ are the induced current density and the magnetic flux density in the

liquid metal, respectively. $k = 1/2\overline{u}' \bullet u'$ is the turbulent kinetic energy, and ε is the dissipation rate. It can be seen that the fluid is affected by the EM field through the Lorentz force while the EM filed is affected by the fluid through the fluid velocity. The interaction between the EM field and the turbulence is more complex, and this coupling effect is only significant when $\mathrm{Re}_m \sim 102$ [11]. In this work, Re_m was less than 10, and this effect was ignored in the simulations. It should be noted that these sets of equations were not attained by default in the used solver. The weak forms of the governing equations for the EM field were modified in order to add the Coulomb's law and the term including the fluid velocity.

2.3. Boundary Conditions and Modeling Settings. The boundary conditions of the simplified ALIP model are shown in Figure 2. It is seen that the flow channel is divided into the EM section and non-EM section. The fluid is only simulated in the annular flow channel while the EM filed is solved in both the flow channel and the air domain. The boundary conditions for the fluid field are straight. A uniform velocity which is calculated based on the simulated flow rate and the cross-sectional area of the annular channel is defined at the inlet. The constant pressure is set at the channel's outlet. The inner and outer surfaces of the flow channel are assumed the no-slip condition. The turbulent kinetic energy and dissipation rate defined at the inlet are calculated based on the fluid velocity and the height of the flow channel.

The boundary conditions for the EM field are defined separately in different sections. In the EM section, the boundary conditions on the inner and outer surfaces of the flow channel are defined using the following set of equations:

$$B_\varphi(r_1) = 0, B_z(r_1) = \mu J_s, \tag{5}$$

$$B_\varphi(r_2) = 0, B_z(r_2) = 0, \tag{6}$$

where r_1 is the radius of the outer surface of the flow channel and r_2 is the radius of the inner surface of the flow channel. J_s is a surface current density imposed on the outer surface. Its detailed description will be presented in the following paragraph. The expressions for defining the EM boundary conditions on the flow channel of ALIP were employed and proved in several previous studies [9, 16, 24]. It can create the induced magnetic field and current density in the liquid metal with reasonable accuracy while the simulations of stators, coiling windings, and ducts can be ignored. In the non-EM section, the magnetic insulation boundary condition $\boldsymbol{n} \times \boldsymbol{A} = 0$ is defined on the boundary of the air domain and the inner surface of the flow channel. However, the boundary of the air domain, which is connected to the boundary of the outer stator (not simulated in this model), should be defined as the ideal magnetic conductor $\boldsymbol{n} \times \boldsymbol{B} = 0$ in order to ensure the computational integrity of the EM field.

The externally imposed surface current density on the outer surface of the flow channel is defined as follows:

$$J_s = J_{s0}\left[1 + \alpha \cos\left(k_{\varphi 1}\varphi + \varphi_1\right)\right] \cos\left(\omega t - k_z + \varphi_0\right), \tag{7}$$

where J_{s0} is the amplitude of the surface current density; $\omega = 2\pi f$ is the angular frequency of the surface current density; k_z is the wave number of the surface current density along the axial direction, and it is defined as $k_z = 2\pi/\lambda_z$ and λ_z L/P; L and P are the length and the number of pole pairs of the EM section; and φ_0 is a prescribed axial phase angle. t and z represent time and axial displacement, respectively. α defines the circumferential nonuniformity of the surface current density or the magnitude of the disturbance. $k_{\varphi 1}$ is the wave number of the surface current density in the azimuthal direction. It is defined as $k_{\varphi 1} = 2\pi/\lambda_\varphi$ and $\lambda_\varphi = 2/N$, where N denotes the cyclic number of the disturbance artificially defined along the channel perimeter, φ is the circumferential angle, and φ_1 is a prescribed circumferential phase angle. The surface current density is applied only in the circumferential direction, and the values in the radial and axial directions are 0 and are only set on the outer surface of the electromagnetic segment, and are zero at other locations. In a real ALIP, the induced magnetic field in the liquid metal is not circular symmetry in most cases. For instance, $k_{\varphi 1} = 1$ and $\alpha = 0.1$ indicate that there is a nonuniform induced magnetic field in the liquid metal due to the installed eccentricity of either the conveying ducts or the stators with its magnitude varying in ±10%. In this work, the numerical model was built with the reference to the real ALIP reported in Ref. [5]. The value of J_{s0} was determined in trial and error so that the simulated pressure at the outlet was consistent with the experimental result. The final values are set as $J_{s0} = 93000$ A/m, $\alpha = 0.1$, $k_{\varphi 1} = 1$, $N = 1$, $k_z = 22.16$ rad/m, $\varphi_0 = \varphi_1 = 0$, and $f = 50$ Hz.

2.4. Mesh Independent Study. The structural mesh scheme was used to discretize the simulation domain. The number of grid points is defined as $N_r \times N_\varphi \times N_z = 12 \times 100 \times 150$. The mesh is refined in the near-wall region, and the distance of the first node from the surface is 0.0002 m so that $y+$ satisfies $30 < y+ < 300$ (see Figure 4). Thus, the standard wall function is applicable in the mesh. Four girds with different refinements were used to study the mesh independence of the numerical model. The degrees of freedom of the four meshes are 8.63, 9.34, 12.48, and 15.45 million, respectively. The numerical model was calculated under the steady-state condition with the flow rate of $q = 5.3\ \mathrm{m}^3$/min. The monitoring points set in the case are at the pump's inlet $z = -0.115$ m, the outlet $z = 0.965$ m and the center of the flow channel $z = 0.425$ m along the centerline ($r = 0.148$ m) of the flow channel. The predicted pressure difference Δp_{em} is defined as the difference between the points at the pump's outlet and inlet. The simulated radial magnetic flux density B_r and the axial Lorentz force $F_{l,z}$ from the point at the center of the flow channel are also compared among different meshes. The values of the compared parameters are presented in Table 2. In the steady-state calculation, the Lorentz

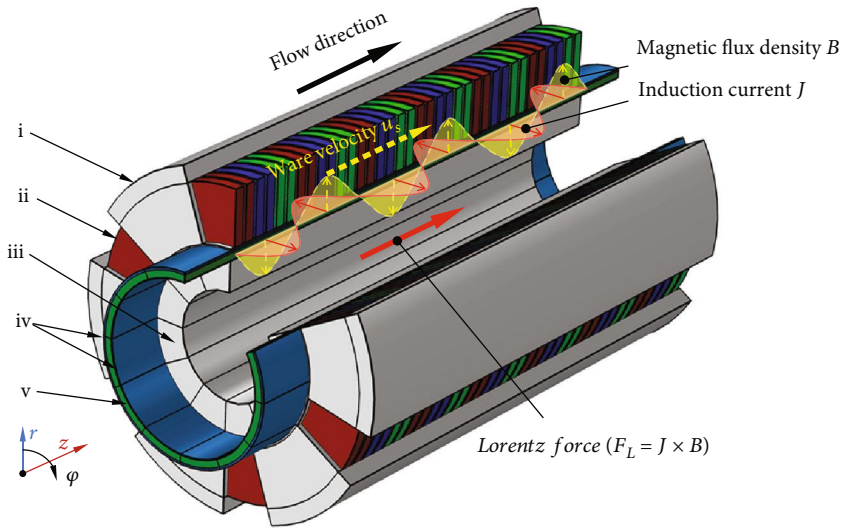

Figure 1: Structural schematic of ALIP: (i) outer stator, (ii) coils zone, (iii) inner stator, (iv) stainless steel ducts, and (v) liquid metal in flow channel [24].

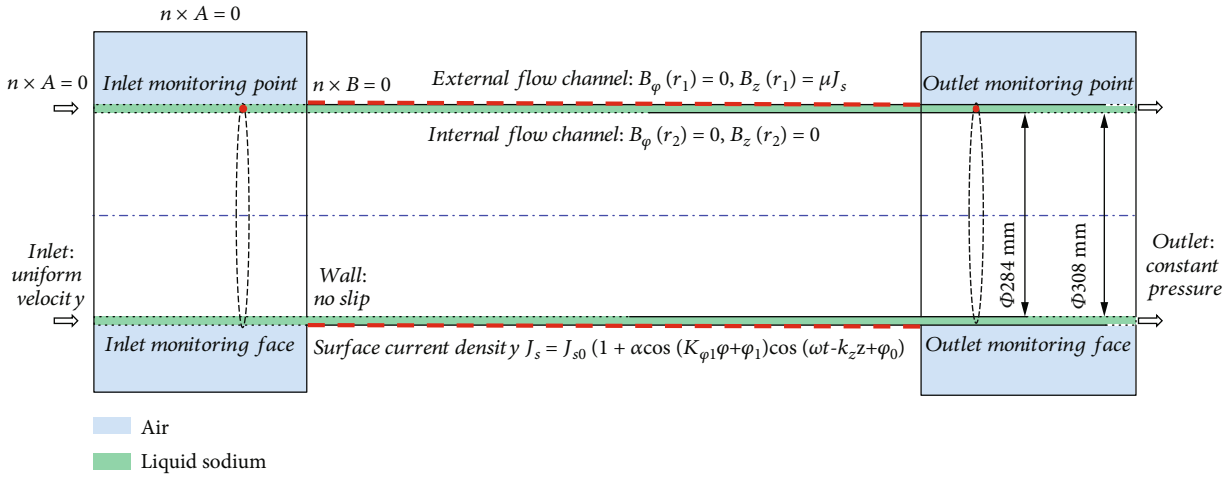

Figure 2: Simulation domain and boundary conditions.

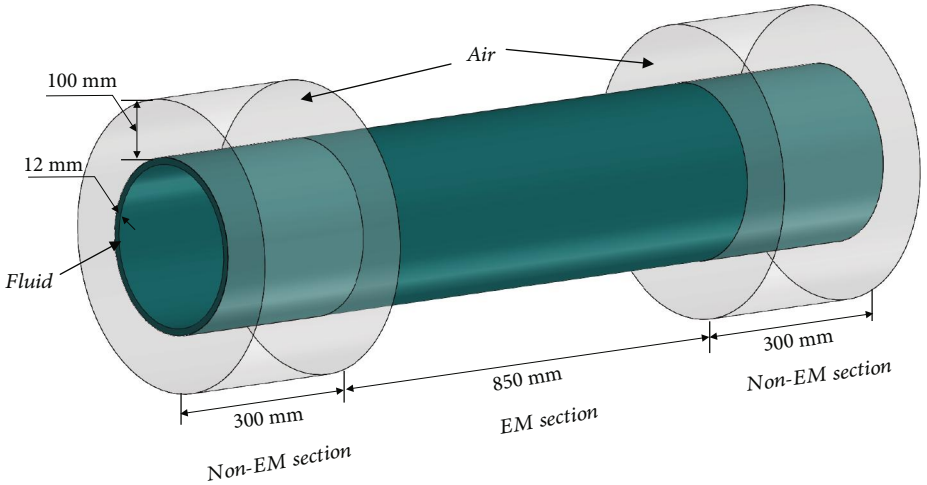

Figure 3: Structural schematic and dimensions of the simplified numerical model.

Table 1: Main parameters of the numerical model (liquid sodium at 220°C) [6].

Parameters	Values
Simulated flow rate Q (m^3/min)	5.3
Radius of the center of the flow channel r (m)	0.148
Height of the flow channel d (m)	0.012
Total length of the ALIP L (m)	1.450
Density of liquid sodium ρ (kg/m^3)	898.25
Conductivity of liquid sodium σ (S/m)	7.3×10^6
Kinetic viscosity of liquid sodium ν (m^2/s)	4.7×10^{-7}
Relative magnetic permeability of liquid sodium	1

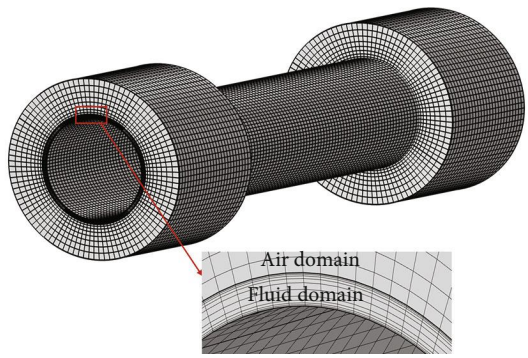

Figure 4: Schematic of the computational mesh.

force under a constant magnetic field always inhibits the flow of liquid metal, so the values of the axial Lorentz force are negative in Table 2. The results show that the maximum error of each parameter among four meshes is less than 1%. However, it is found that the results of all parameters are monotonously changed from mesh #1 to mesh #3, and therefore, mesh #3 is selected for the following study.

2.5. Model Validation. The numerical model was validated by comparing the simulated pressure difference with the experimental result reported in Ref. [24]. The simulations were performed under seven flow rates, which are 2.0, 3.4, 4.0, 4.4, 5.0, 5.3, and 7.0 m^3/min. The simulation time was 0.8 s, which is equivalent to 40 current cycles. It was found that the pressures at the inlet and outlet of the EM section could be stable after the initial 10 cycles. The pressures at the inlet and outlet were obtained by averaging the pressure on the cross-sections of the annular channel, which are illustrated in Figure 2. Then, the area-averaged pressure was time averaged from 0.2 s to 0.6 s. The pressure differences obtained at different flow rates are depicted in Figure 5(a), and they are compared with the experimental results. The figure shows that the simulation results have good agreement with the experimental results. More importantly, a "hump" phenomenon on the curve of pressure difference versus flow rate has been reproduced in the simulation. The comparison has shown that the numerical model could accurately predict the fluid field and the associated pressure difference at both the nominal and off-design flow rates, and it can be used to simulate the unstable flows at the off-design working conditions.

The pressure pulsation predicted by the numerical model was also validated with the experimental value. The transient area-averaged pressure at the outlet at $q = 5.3\ m^3$/min was extracted from 1.2 s to 3.2 s, and the fluctuating pressure was converted into frequency domain as shown in Figure 5(b). $q = 5.3\ m^3$/min was selected as the working condition in the following study for active flow control, because it is the critical point for the large-scale vortex flow in the flow channel to occur. The simulation time at this flow rate was extended to 3.2 s in order to enrich the data for the time history of the pressure pulsation at the pump's outlet. In Figure 5(b), δp denotes the magnitude of the pressure pulsation, and Δp_{em} denotes the pressure difference between the inlet and outlet of the EM section. The figure shows that the simulation result has good agreement with the experimental result at both the low (~1 Hz) and high (100 Hz) frequencies. The pressure pulsation of the low frequency is caused by the large-scale unstable flows while that of the high frequency is the well-known pulsation of DSF.

3. Results and Discussion

3.1. Active Flow Control Method. As analyzed in the previous study [24], the flow behavior is governed by the competition between the pressure gradient and the induced Lorentz force. When there is a small disturbance in the magnetic field or the fluid, the inherent magnetic-fluid coupling effect will amplify the disturbance and eventually form the large-scale vortex. The flow in the zone of lower axial velocity has to sacrifice its kinetic energy (i.e., velocity) to compensate the deficiency in the work done by the low Lorentz force in this region. The flow streamlines of an instant on the middle φ-z plane of the flow channel with $r = 0.148$ m at $q = 5.3\ m^3$/min is shown in Figure 6 in order to better illustrate these unstable flows. It is seen that a pair of vortices appears in the azimuthal region of $0.5\pi < \varphi < 1.5\pi$ and the vortices occupy almost the whole EM section along the axial direction. However, the flow is unstable, and the vortex is evolved in cyclic way. The periodical occurrence of the large-scale vortex is the reason for the pressure pulsation of low frequency at the ALIP's outlet.

In this work, an active flow control method was proposed to suppress the unstable flows in the flow channel. Since it is found that the vortical region corresponds to low Lorentz force due to small disturbance in the fluid and magnetic field, an extra magnetic field is tried to be imposed on the original one, and an enhancement of the magnetic field is obtained in the vortical region. This method is expected to increase the local low Lorentz force and compensate the deficiency without sacrificing the fluid kinetic energy. Here, the additive magnetic field is referred to as the modulated magnetic field, and the original magnetic field is referred to as the background magnetic field.

Like the background magnetic field, the modulated magnetic field in the flow channel can be stimulated by imposing

Table 2: Verification of mesh independence.

	Degree of freedom	Δp_{em} (Pa)	B_r (T)	$F_{l,z}$ (N/m^3)
Mesh #1	8629487	-296094	0.081038	-539658
Mesh #2	9340452	-297152	0.081051	-539820
Mesh #3	12480045	-297548	0.081062	-540073
Mesh #4	15452941	-297287	0.081053	-539868
Relative error		0.491%	0.0296%	0.0769%

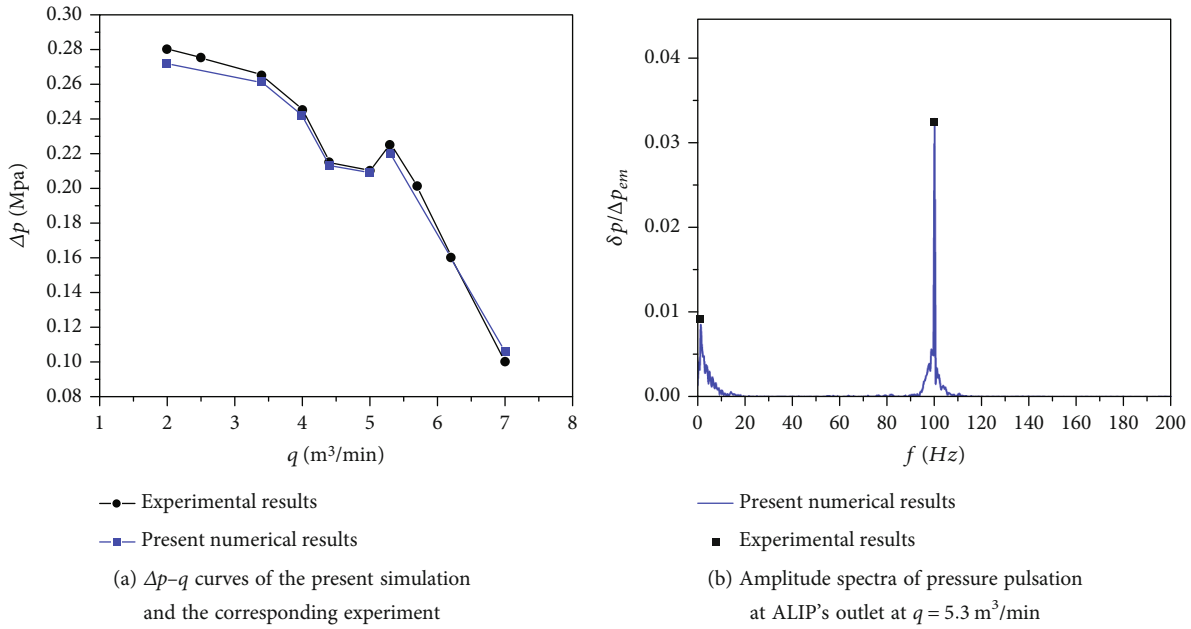

(a) Δp–q curves of the present simulation and the corresponding experiment

(b) Amplitude spectra of pressure pulsation at ALIP's outlet at $q = 5.3$ m^3/min

Figure 5: Comparison of the simulation and experimental results.

a harmonic surface current density. The modulated surface current density J_{sm} is defined as follows:

$$J_{sm} = J_{s0}\beta \cos\left(k_{\varphi 2}\varphi + \varphi_2\right) \cos\left(\omega t - k_z z + \varphi_0\right), \quad (8)$$

where β is a strength factor, which represents the ratio of the amplitude of J_{sm} to the amplitude of J_s. $\omega = 2\pi f$ is the angular frequency of the surface current density, k_z is the wave number of the surface current density along the axial direction, and $k_{\varphi 2}$ is the wave number of the modulated surface current density in the azimuthal direction, which is defined as $k_{\varphi 2} = 2\pi/\lambda_\varphi$ and $\lambda_\varphi = 2/N$, where $N = 1$ is the cyclic number of disturbance and φ_2 is the prescribed circumferential phase angle. To reduce the interference of the modulated surface current density with the original surface current density, Equation (9) will be only added in the vortical zone.

The vortical region as shown in Figure 5 illustrates that its azimuthal range is $0.5\pi < \varphi < 1.5\pi$, and its axial range is approximately $0\,\text{m} < z < 0.85\,\text{m}$. Therefore, the modulated magnetic field should be loaded in this region. The modulated surface current density J_{sm} is still imposed on the outer surface of the flow channel. By combining the modulated

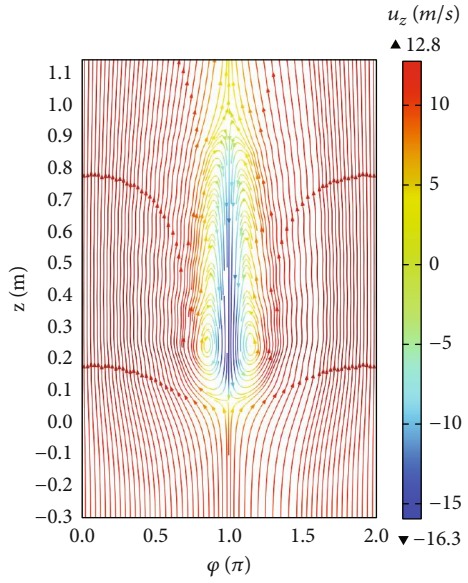

Figure 6: Flow streamlines on the middle φ - z plane of the flow channel at $q = 5.3$ m^3/min.

Table 3: Parameters' values of the modulated surface current densities.

	J_0 (A/m)	α	β	$k_{\varphi 1}$	φ_1	$k_{\varphi 2}$	φ_2	ω (Hz)	k_z	φ_0
J_{s1}	0.93×10^5	0.1	0	1	0	1	0	314	22.472	0
J_{s2}	0.93×10^5	0.1	0.1	1	0	1	π	314	22.472	0
J_{s3}	0.93×10^5	0.1	0.3	1	0	1	π	314	22.472	0

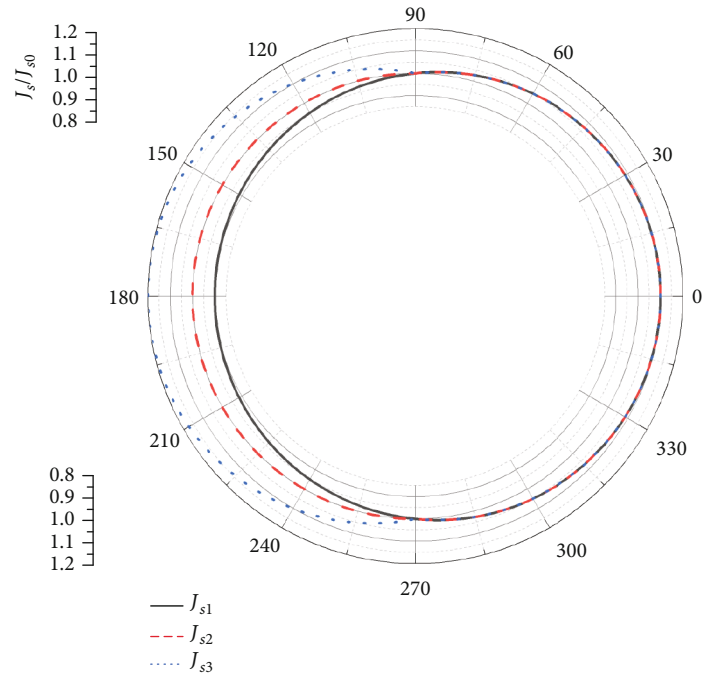

Figure 7: Circumferential distribution of the modulated surface current density.

surface current density, the externally imposed surface current density is defined as follows:

$$J_{sm} = \begin{cases} J_{s0}\left[1 + \alpha \cos\left(k_{\varphi 1}\varphi + \varphi_1\right) + \beta \cos\left(k_{\varphi 2}\varphi + \varphi_2\right)\right] \cos\left(\omega t - k_z + \varphi_0\right), \text{vortex zone}, \\ J_{s0}\left[1 + \alpha \cos\left(k_{\varphi 1}\varphi + \varphi_1\right)\right] \cos\left(\omega t - k_z + \varphi_0\right), \text{nonvortex zone}. \end{cases} \quad (9)$$

It is seen that the modulated surface current density is only added in the vortex zone. To investigate the effect of the strength of the modulated magnetic field on suppressing the large-scale vortex flow, the strength factor β is set as 0.1 and 0.3. Therefore, three surface current densities (J_{s1}, J_{s2}, and J_{s3}) were defined and simulated in this work. The azimuthal profiles of the simulated surface current densities at a fixed time and axial position are shown in Figure 6. The amplitude is divided by the amplitude of J_{s0} without any disturbance ($\alpha = \beta = 0$). Table 3 presents the values of the parameters of J_{s1}, J_{s2}, and J_{s3}. J_{s1} follows the basic form of J_{s0} and adds a circumferential disturbance which could be introduced by the installed eccentricity of the stator or the conveying duct. It is seen in Figure 7 that the profile of J_{s1} appears eccentric in the azimuthal direction. J_{s1}/J_0 is smaller than 1 in $0.5\pi < \varphi < 1.5\pi$, while it is larger than 1 in $0 < \varphi < 0.5\pi$ and $1.5\pi < \varphi < 2\pi$. J_{s2} inherits all the parameters of J_{s1} while it is combined with a modulated surface current density with the strength factor of 0.1. The modulated surface current density is only activated in $0.5\pi < \varphi < 1.5\pi$ in order to enhance the local magnetic field. J_{s3} combines a modulated surface current density with the strength factor of 0.3 at the same region. It is seen that J_{s2}/J_0 and J_{s3}/J_0 can be increased to 1.0 and 1.2 at the azimuthal angle of π, respectively. After defining the modified surface current density, the numerical model of the ALIP

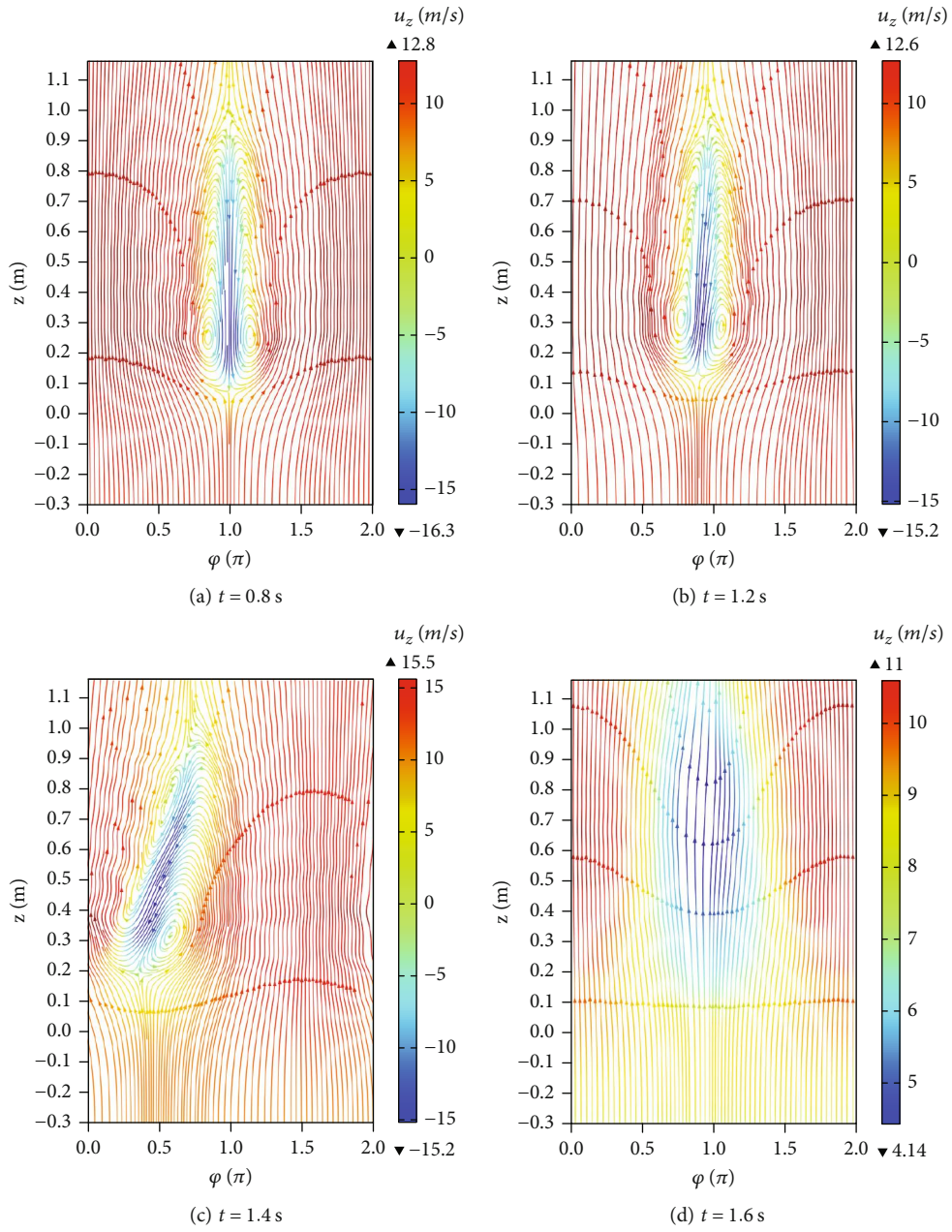

Figure 8: Continued.

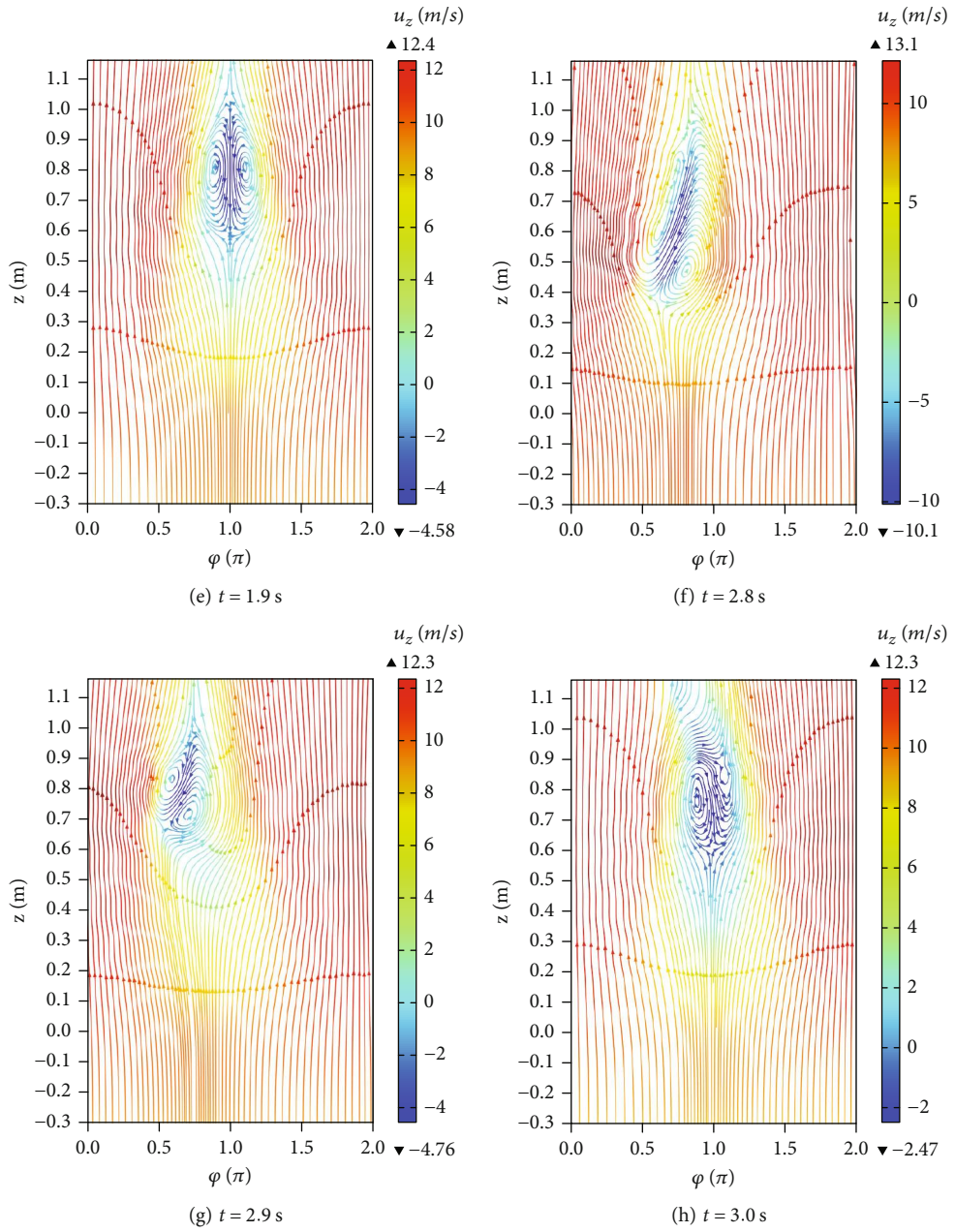

Figure 8: Continued.

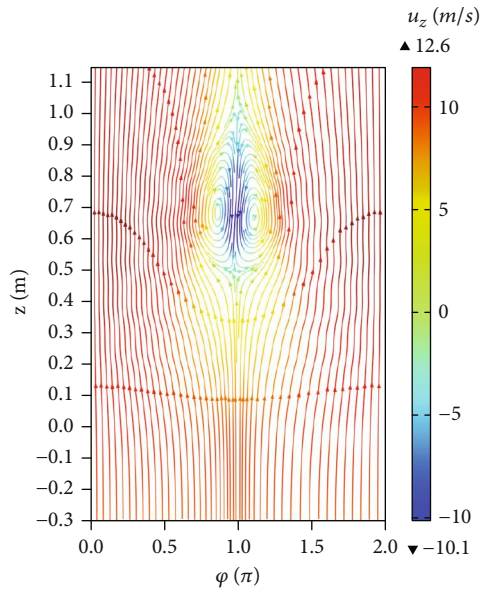

FIGURE 8: Time evolution of flow pattern in the flow channel under J_{s1} condition.

was simulated at $q = 5.3\ \mathrm{m}^3/\mathrm{min}$, where vortex occurred in the flow channel. The simulation time was set as 3.2 s while the data processing began at $t = 0.8$ s.

3.2. Influence of the Active Flow Control on the Flow Field. The behavior of the MHD flow within the active flow control was studied based on the simulation. The flow streamlines are depicted on the middle circumferential plane (φ-z section and $r = 0.148$ m) of the flow channel. A pair of vortices was symmetrically formed in the central region of the plane at $t = 0.8$ s when the MHD flow had undergone the initial development. Then, the defined different surface current densities were imposed and simulated in the numerical model. The effect of the modulated surface current density on the flow pattern was revealed based on the simulation results.

A series of instants with distinct flow characteristics were picked up, and the transient flow streamlines are illustrated in Figures 8(a)–8(i) under the J_{s1} condition. A pair of vortices was presented constantly in the flow channel, covering $0.05\ \mathrm{m} < z < 0.9\ \mathrm{m}$ in the axial direction and $0.7\pi < \varphi < 1.4\pi$ in the azimuthal direction. Thus, the size of the vortical zone occupies the whole EM-section and one third width of the flow channel. The vortices are frozen until $t = 1.2$ s when the symmetrical axis of two vortices begins to shift to the left side. From $t = 1.2$ s to $t = 1.6$ s, the pair of vortices moves toward the left edge of the domain, and then, they are vanished in the flow channel. The results indicate that the vortex flow can lose its stability and swing to the area of strong magnetic field. The associated strong Lorentz force will diminish the deficiency in the Lorentz force and cause the collapse of the vortex. During the period of $t = 1.6 \sim 1.9$ s, a new pair of vortices is gradually formed in the original position, and they grow to the size of covering the whole EM-section. At $t = 2.8$ s, the vortices move toward the left edge of the domain again. From $t = 2.9$ s to $t = 3.0$ s, the previous vortices are vanished and a new pair of vortices is formed in the original position. At $t = 3.2$ s, the new pair of vortices becomes stable and they are growing with time. The results show that the vortex evolution is periodic with a cycle time of approximately 1 s.

The flow streamlines at different instants under the J_{s2} working condition are shown in Figures 9(a)–9(l). The modulated surface current density aiming at compensating the deficiency in the Lorentz force is imposed on the original surface current. It is seen that the symmetrical axis of two vortices begins to shift at $t = 1$ s and the vortices are vanished in the flow channel at $t = 1.3$ s. A new pair of vortices is well formed at $t = 1.4$ s. They gradually grow until $t = 1.7$ s when the symmetrical axis begins to shift again. The new pair of vortices is vanished again at $t = 2.1$ s. Another pair of vortices is formed at $t = 2.2$ s, and they grow until $t = 2.6$ s when the symmetrical axis begins to shift again. From $t = 2.7$ s to $t = 2.8$ s, the third cycle of the pair of vortices is accomplished and a new cycle begins. The results illustrate that the vortex evolution is periodic with a cycle time of approximately 0.7 s. The modulated surface current accelerates the evolution rate. Moreover, it is found that the vortex size is also reduced. For instance, the vortical zone occupies $0.25\ \mathrm{m} < z < 0.97\ \mathrm{m}$ in the axial direction and $0.8\pi < \varphi < 1.3\pi$ in the azimuthal direction at $t = 1.7$ s when the vortices are fully developed in the flow channel. The time interval from collapse to regeneration of the vortices is also shortened to about 0.1 s while it needs more than 0.3 s under J_{s1} condition.

The flow streamlines at different instants under the J_{s3} working condition are shown in Figures 10(a)–10(k). The modulated surface current density is intensified by changing

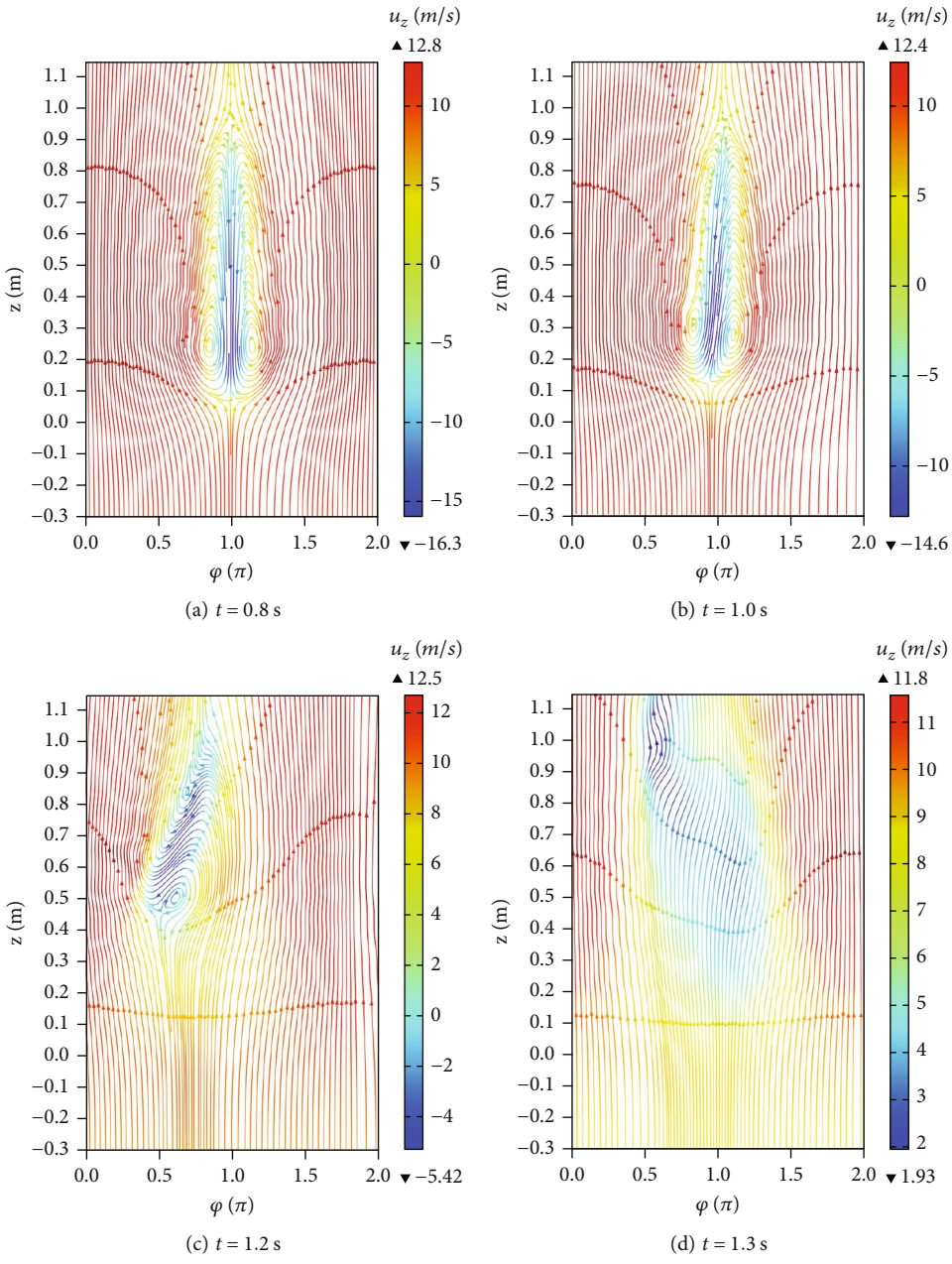

Figure 9: Continued.

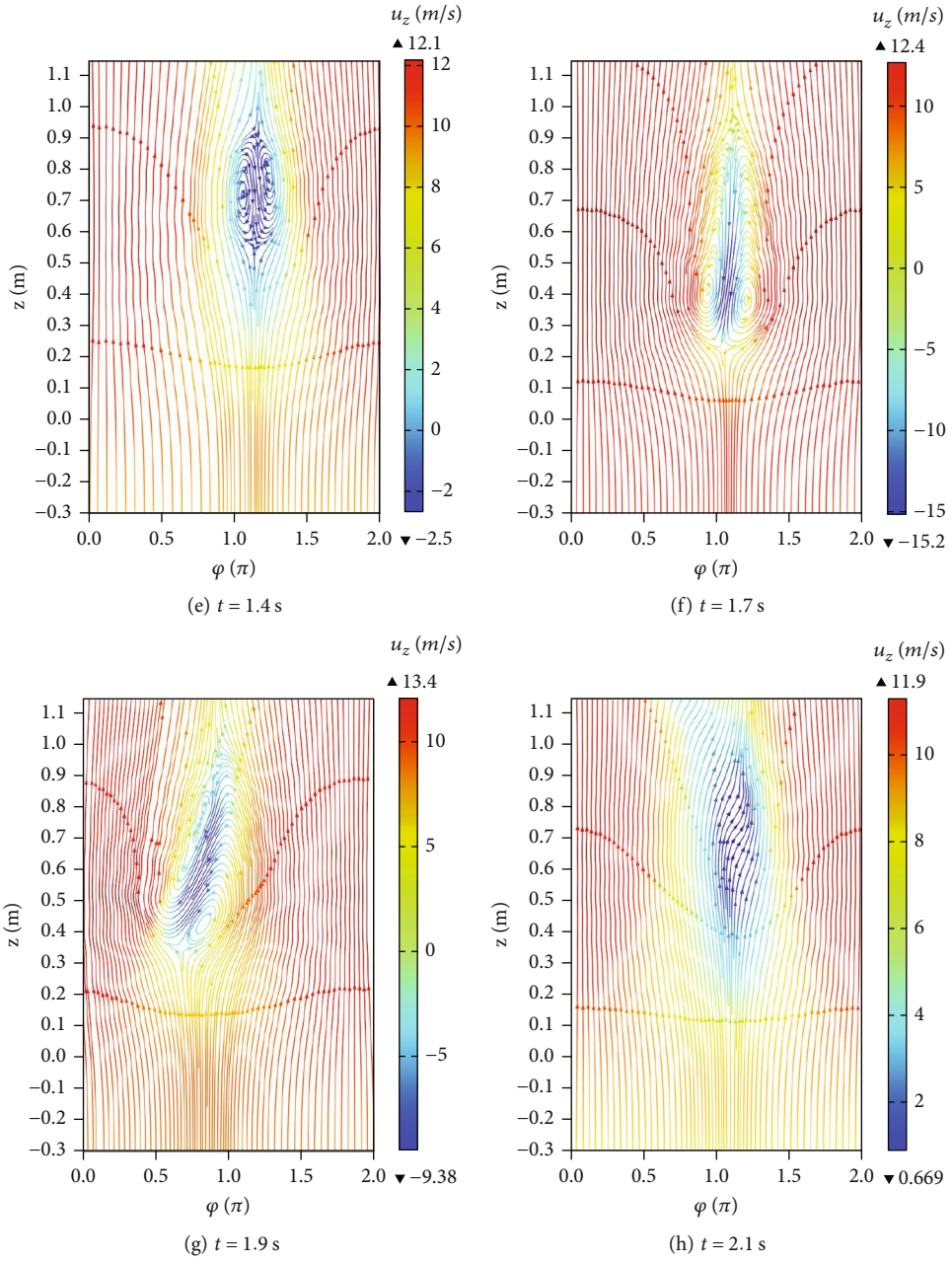

(e) $t = 1.4$ s (f) $t = 1.7$ s

(g) $t = 1.9$ s (h) $t = 2.1$ s

Figure 9: Continued.

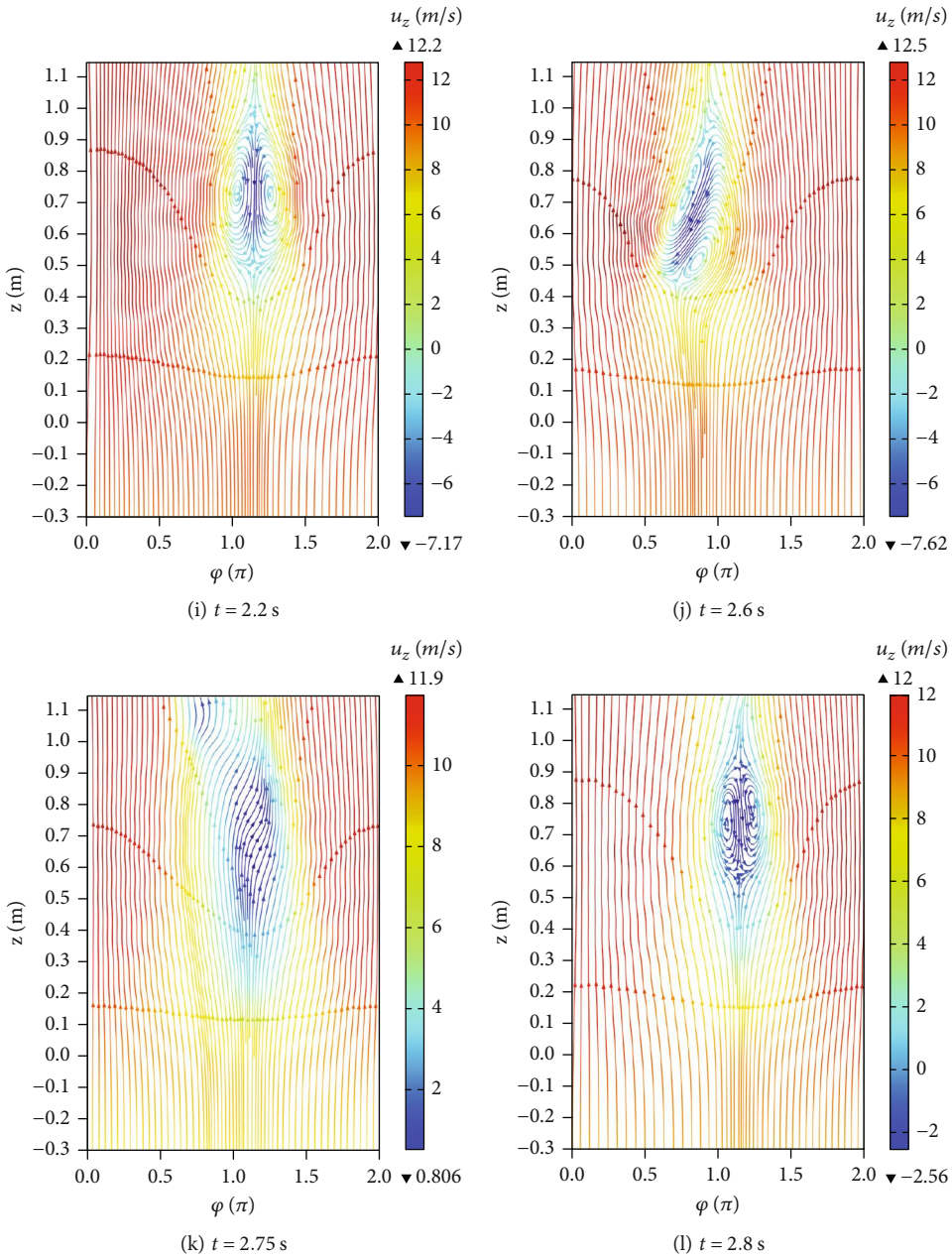

FIGURE 9: Time evolution of flow pattern in the flow channel under J_{s2} condition.

the strength factor from 0.1 to 0.3. It is seen that the original pair of vortices breaks down into several small vortices at $t = 1.0$ s under the strong modulated surface current. They are evolved into two vortices again at $t = 1.2$ s. Then, they gradually move to the right side, and the symmetry of two vortices is vanished. The collapse and regeneration of the vortices are accomplished in the period of $t = 1.6 \sim 1.7$ s. It is found that the collapse of the previous vortices and the regeneration of new vortices are simultaneously formed in the flow channel as shown in Figures 10(d)–10(f). After that, a tilting pair of vortices is constantly presented in the flow channel from $t = 1.8$ s to $t = 2.5$ s, during which the vortices are fully developed. The vortices break down again into smaller vortices at $t = 2.7$ s, and they are evolved into a pair of vortices again at $t = 2.9$ s. After that, the vortices are evolved between a pair of vortices and several smaller vortices, waiting for the next cycle of collapse and regenerate. The results illustrate that the modulated surface current cannot further accelerate the evolution rate. However, the vortex size is continuously reduced. For instance, the vortical zone occupies the region of $0.9\pi < \varphi < 1.35\pi$ and $0.35\,\text{m} < z < 0.95\,\text{m}$ at $t = 2.5$ s when the vortices are fully developed in the flow channel. The time interval from collapse to regeneration of the vortices is also shortened to less than 0.1 s (e.g., $t = 1.6 \sim 1.7$ s). Another important finding is that the collapse of the previous vortices and the regeneration of new vortices are formed without any time interval, as shown in Figure 9(e).

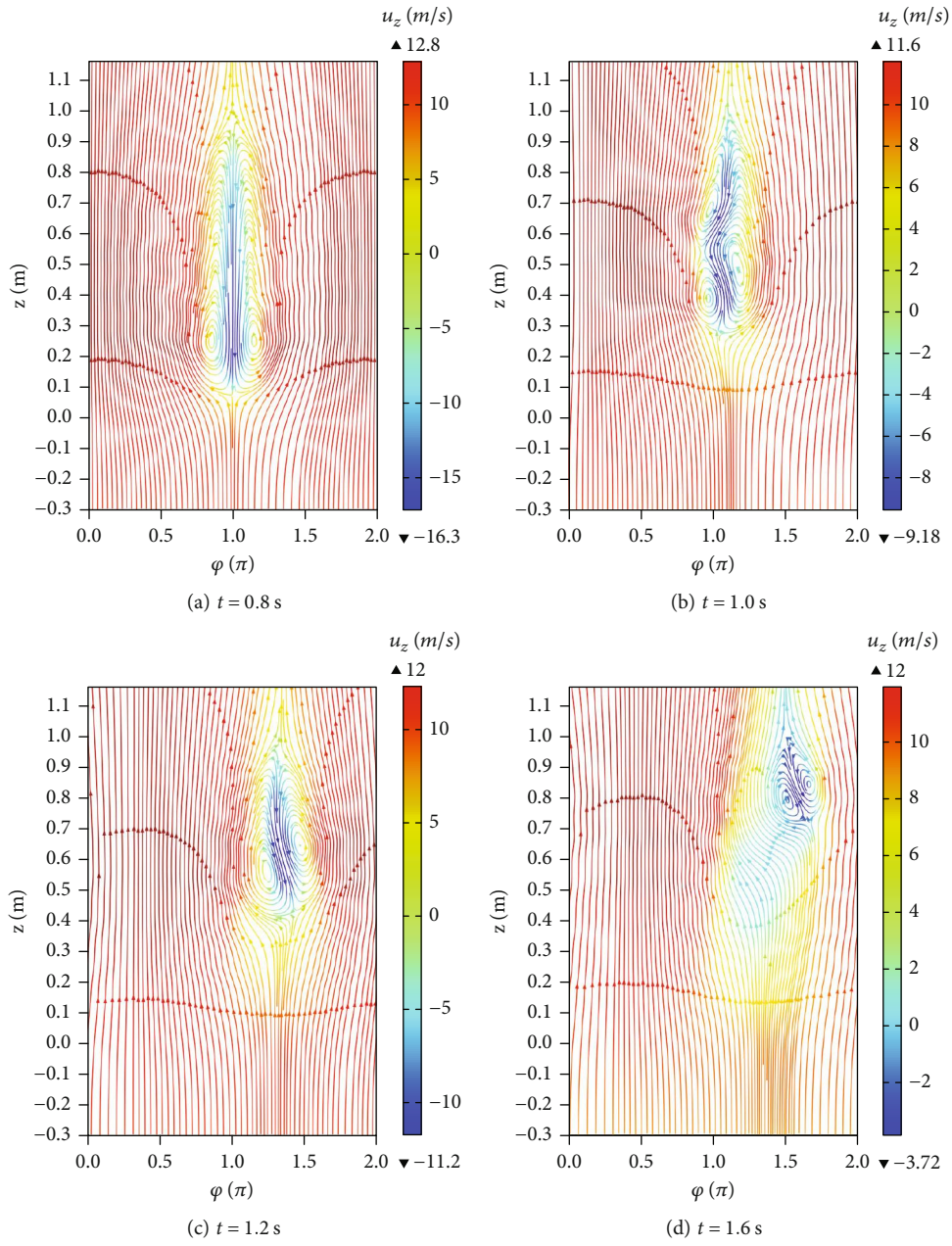

Figure 10: Continued.

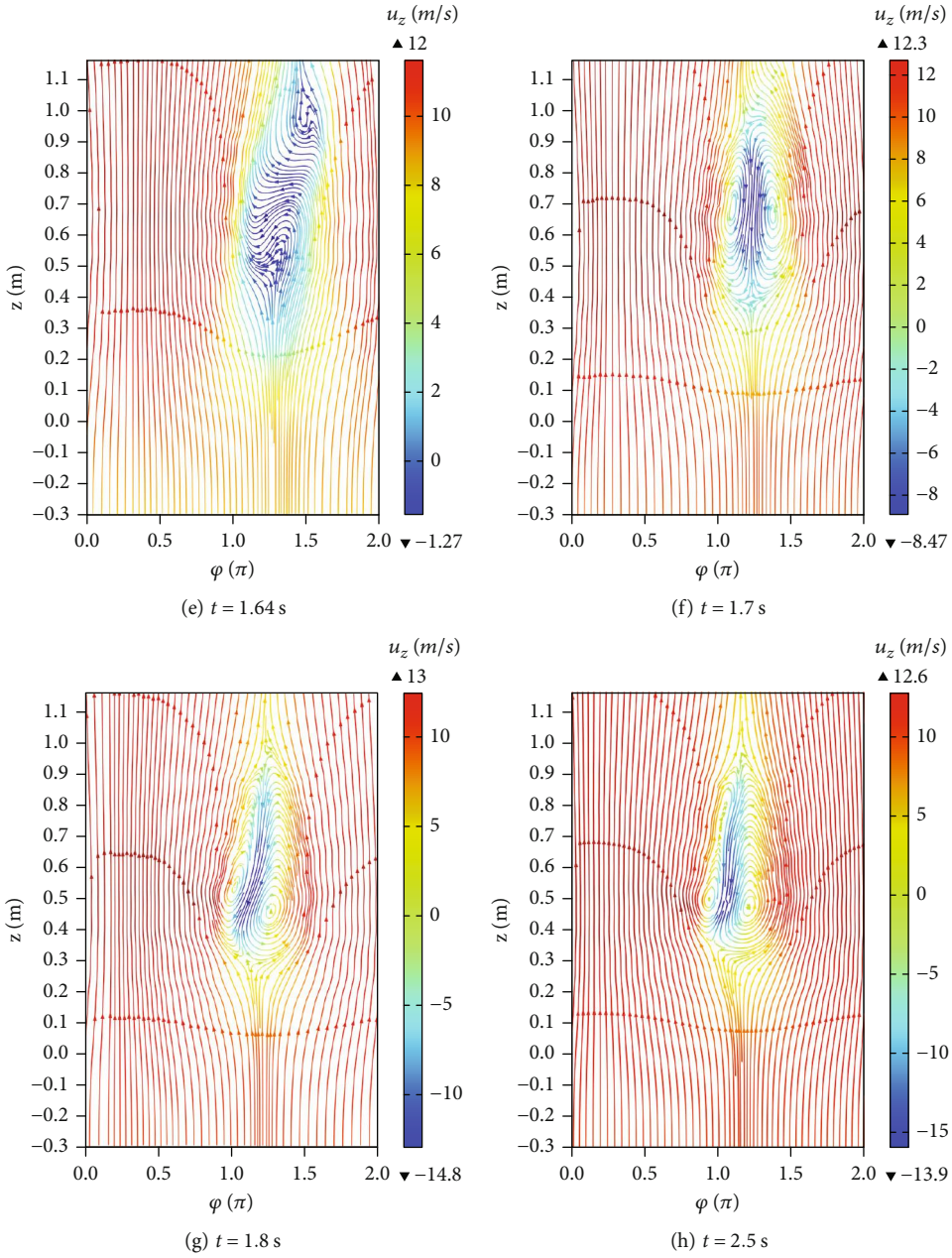

Figure 10: Continued.

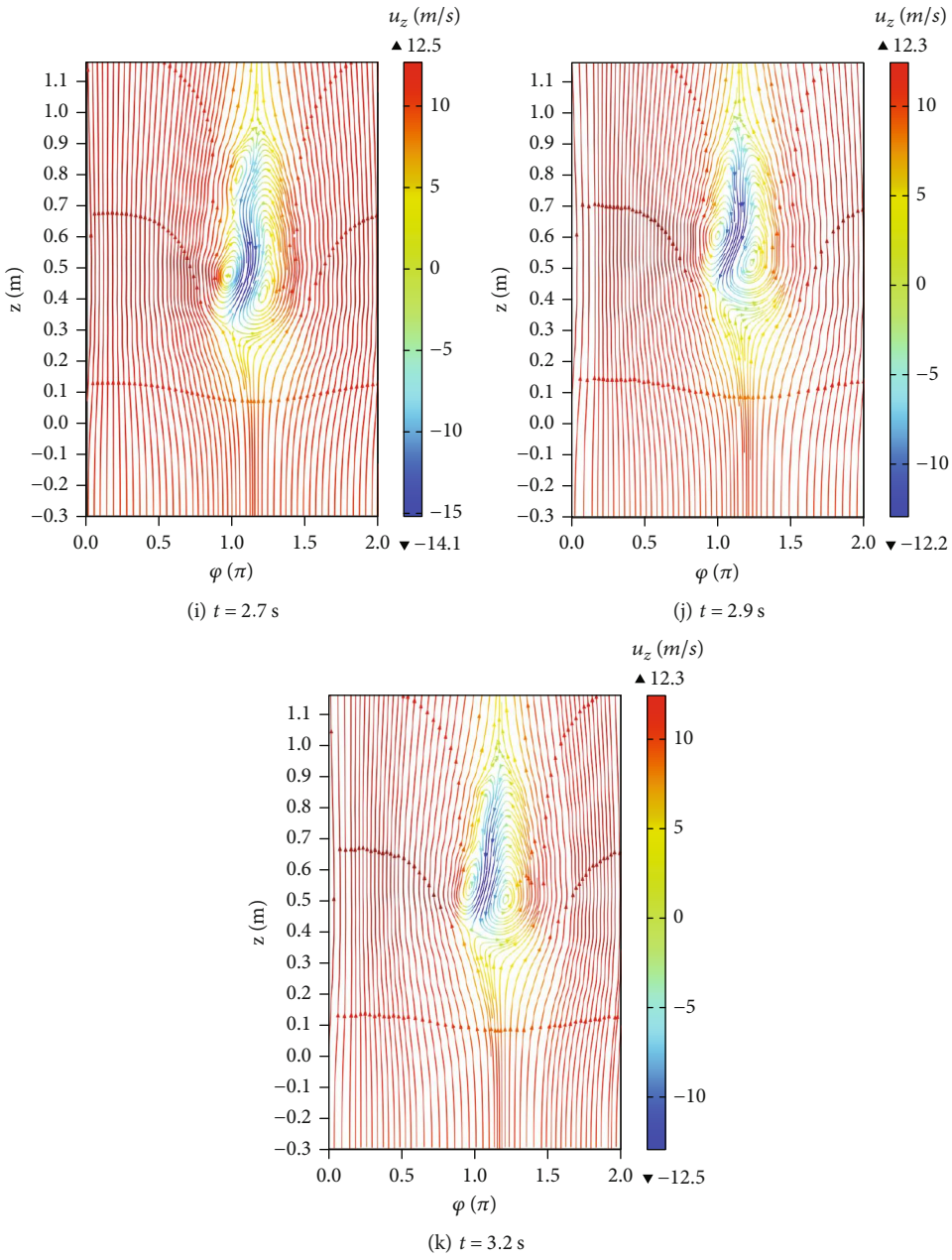

FIGURE 10: Time evolution of flow pattern in the flow channel under J_{s3} condition.

The strength of the vortices is also estimated under different J_s conditions by using the Q-criterion [33–36]. The Q values of the vortices in the full development are presented in Figure 11. It is seen that the maximum value of Q is $1.32 \times 10^4\ S^{-2}$, $6.17 \times 10^3\ S^{-2}$, and $5.72 \times 10^3\ S^{-2}$ under the J_{s1}, J_{s2}, and J_{s3} conditions, respectively. Thus, the strength of the vortices is significantly reduced after introducing the modulated surface current. This reduction will also benefit in reducing the undesirable current induced in the vortical zone and the associated energy dissipation of Joule heating.

The time histories of the flow streamline under three surface current densities demonstrate that the modulated surface current density can effectively reduce the size and strength of the large-scale vortices. Also, the time interval between the collapse of the previous vortices and the regeneration of the new vortices is continuously shortened. It is found that there is no time interval under the J_{s3} condition. These improvements in the flow field will directly affect the pressure pulsation at the pump's outlet and the processes of energy conversion in the ALIP.

3.3. Influence of the Active Flow Control on the Pressure Pulsation. Pressure pulsation is one of the key indicators in the stability analysis of ALIP. It has been found that the severe pressure pulsation of low frequency at the pump's outlet is directly related to the large-scale vortices in the flow channel. In this section, the pressure differences at the inlet and outlet of the EM section Δp_{em} under the different

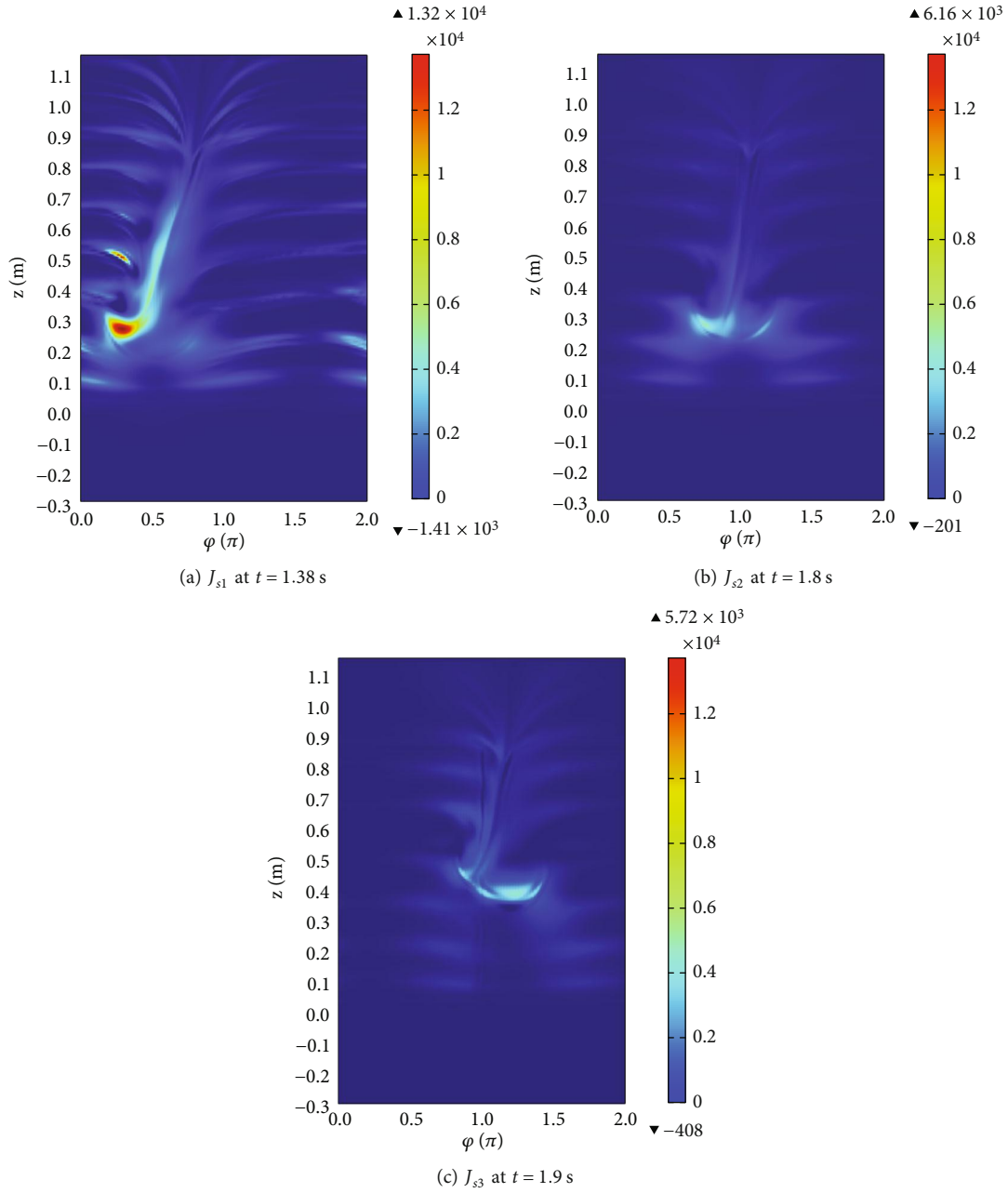

Figure 11: Contours of the Q's value in the middle φ-z plane of the flow channel under J_{s1}, J_{s2}, and J_{s3} conditions.

stimulated surface current densities are presented in Figure 12 from $t = 1.2$ s to $t = 3.2$ s (the time period of $t = 0.8 \sim 1.2$ s is ignored since the initial stage of imposing the modulated surface current density should not be considered). It is seen that the pressure difference is fluctuated with time for all cases and the fluctuations of J_{s2} and J_{s3} are in more regular manner than that of J_{s1}. Besides the fluctuation within short time interval (corresponding to the pulsation of DSF), it is also seen that the pressure difference is fluctuated with the average value over long time interval.

In the second step, the pressure pulsations were processed using the fast Fourier transformation (FFT) method, and the results are illustration in Figures 13(a)–13(c). The x-axis is the frequency, and the y-axis is the ratio of the magnitude of pressure pulsation to the pressure difference. Now, it is clear that there are two main frequencies for the pressure pulsation. The frequency $f = 100$ Hz, which is twice of the frequency of the surface current density, is the well-known pressure pulsation of DSF. It is caused by the sudden interruption of the induced magnetic field at both ends of the EM section of ALIP. The other pressure pulsation is of very low frequency (approximately to 1 Hz). It is seen that the pressure pulsation of low frequency at J_{s1} is 6%. It shows a slight reduction to 5% at J_{s2}. However, when J_{s3} is used in

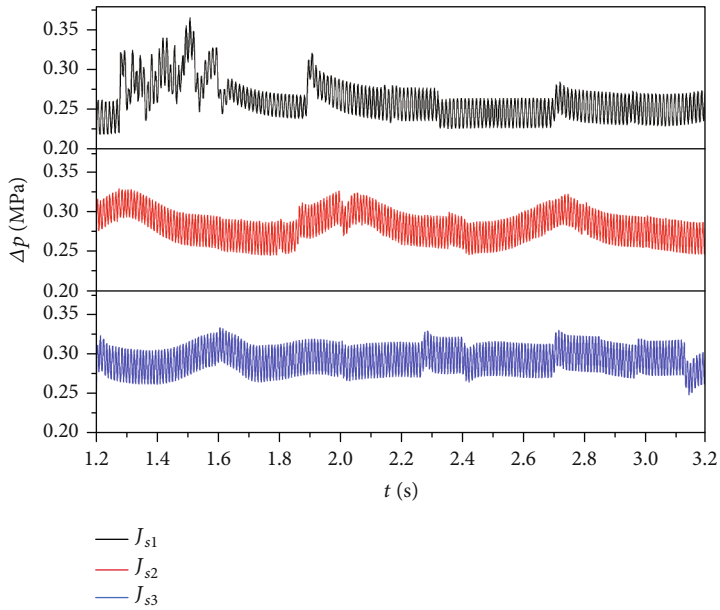

Figure 12: Time history of the pressure difference between the ALIP's inlet and outlet under J_{s1}, J_{s2}, and J_{s3} conditions.

the pump, the pressure pulsation shows a significant reduction to less than 1.2%. Considering the value of Δp_{em} at $q = 5.3\,\mathrm{m}^3/\mathrm{min}$ is 0.31 MPa, the pressure pulsation at J_{s3} condition is around 3.7 kPa while this pulsation at J_{s1} is as high as 18.6 kPa. As for the pressure pulsation of DSF, it is slightly varied in the different simulation cases. The results demonstrate that the modified magnetic field can effectively suppress the pressure pulsation of low frequency if the strength of the modulated surface current density reaches a certain level. If the modulated surface current density J_{s3} is imposed, the pressure pulsation of low frequency can be reduced to an acceptable level.

3.4. Influence of the Active Flow Control on the Energy Conversion. The input energy of ALIP comes from an external power source, and it is transformed into the magnetic field by the magnetic excitation parts. Then, a part of energy in the magnetic field is transferred into the fluid by the work of Lorentz force. Finally, the energy in the fluid is converted into the fluid pressure energy and other fluid-related energies. In this work, we used the governing equations of the magnetic energy and fluid kinetic energy to analyze the energy conversion in the ALIP. The influence of the active flow control on the energy conversion can be estimated.

The equation for the magnetic energy conversion is expressed as follows:

$$\frac{dE_B}{dt} = \int \frac{\boldsymbol{B}}{\mu}\frac{\partial \boldsymbol{B}}{\partial t}dV = \underbrace{-\frac{1}{\mu}\int \boldsymbol{u}\bullet[(\nabla\times\boldsymbol{B})\times\boldsymbol{B}]dV}_{P_{LF}} \underbrace{-\frac{m}{\mu}\int(\nabla\times\boldsymbol{B})^2 dV}_{P_D} + \underbrace{\frac{m}{\mu}\int \boldsymbol{B}\times(\nabla\times\boldsymbol{B})dS}_{P_I}, \tag{10}$$

where $m = 1/\mu\sigma$, E_B is the magnetic energy, and $\boldsymbol{B}$ is the magnetic flux density. The temporal change of the magnetic energy is determined by the three terms on the right-hand side (RHS) of the equation in the second line. P_{LF} is the work of Lorentz force, P_D is the ohmic dissipation in the fluid, and P_I is the input work from the external magnetic field through the boundary. For the current numerical model, the external magnetic energy was obtained by integrating this term over the outer surface of the flow channel overlapping with the surface current density. The other terms were obtained by integrating the terms over the whole fluid domain.

The time histories of the different terms in the equation are illustrated in Figure 14 under three different surface current densities. To eliminate the local fluctuation due to the harmonic current, each term was time averaged over 0.1 s (5 current cycles) in the period time of $t = 0.8 \sim 1.8$ s. Therefore, 10 data points were obtained, and they were smoothed and fitted by the B-spline method. The results show that the time variation of the magnetic energy is much smaller than the variations of other terms. By viewing the average values of the different terms, it is shown that approximately 55% of the external magnetic energy input P_I is converted into the work of Lorentz force P_{LF}, while the rest is still dissipated in the form of ohmic dissipation P_D. It is also shown that P_{LF}, P_D, and P_I under J_{s1} condition suffer from large fluctuations. The fierce variations are strongly related to the flow evolution presented in Section 3.2. As mentioned above, the large-scale vortices in the flow channel have undergone the inception, development, annihilation, and renaissance. Such periodic behavior causes the large fluctuations in the various mechanisms of energy conversion. When the modified surface current densities, i.e., J_{s2} and J_{s3}, are imposed, the most visible change is that the fluctuations in the various mechanisms of energy conversion become more gentle. This change is also explained by the changes in the flow

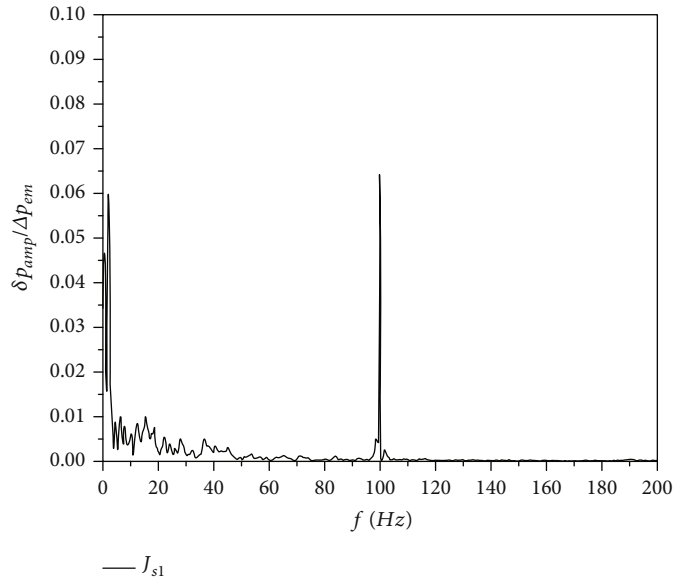

(a) Pulsation spectrum at the J_{s1} working condition

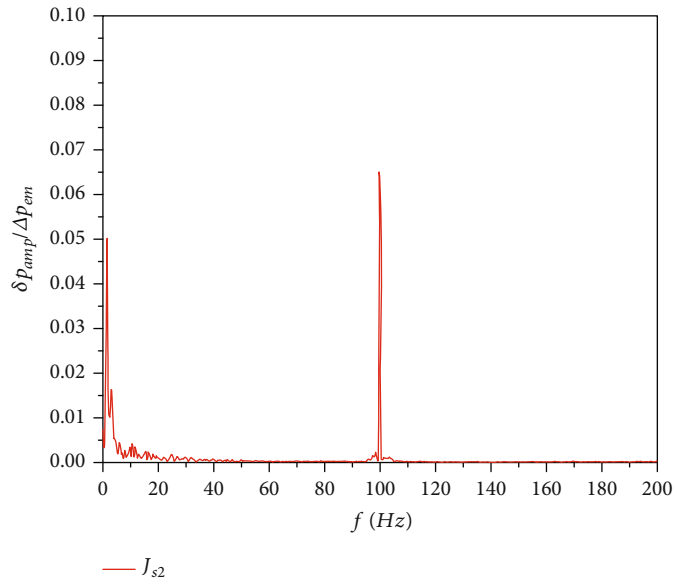

(b) Pulsation spectrum at the J_{s2} working condition

Figure 13: Continued.

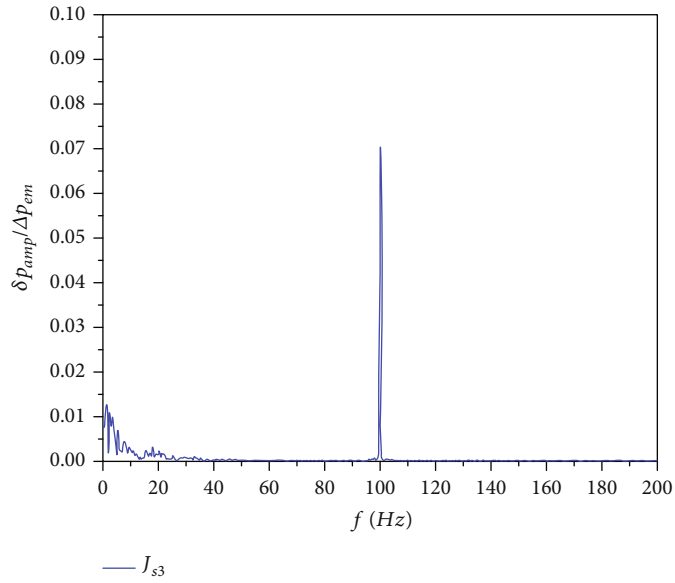

(c) Pulsation spectrum at the J_{s3} working condition

FIGURE 13: Pulsation spectrum of the pressure difference of the ALIP under J_{s1}, J_{s2}, and J_{s3} conditions.

behaviors. The evolution rate of the vortex flow is accelerated, and its strength is weakened by the modified surface current density. The influence of the periodically evolved vortex on the fluctuation of energy conversion is attenuated. In general, the energy powers of different terms are gradually increased as the surface current density is changed from J_{s1} to J_{s3}, because an extra input energy is required in the modulated surface current density.

The work of Lorentz force is the term for putting the magnetic energy into the fluid, which is then converted into the energies in the forms of pressure energy, kinetic energy, and vortex energy of the fluid. The equation for the energy conversion in the fluid is expressed as follows:

$$\frac{1}{\mu}\int \boldsymbol{u}\bullet[(\nabla\times\boldsymbol{B})\times\boldsymbol{B}]dV = \int \boldsymbol{u}\bullet\boldsymbol{F_L}dV = \underbrace{\int \nabla\bullet(\boldsymbol{u}p)dV}_{P_p} + \underbrace{\rho\int \nabla\bullet\left(|\boldsymbol{u}|^2\frac{\boldsymbol{u}}{2}\right)dV}_{P_k} + \underbrace{\upsilon\rho\int \nabla\bullet(\boldsymbol{\omega}\times\boldsymbol{u})dV}_{P_{VF}} + \underbrace{\upsilon\rho\int \boldsymbol{\omega}^2 dV}_{P_{En}} + \rho\frac{dK}{dt}, \tag{11}$$

where $K = 1/2\int |\boldsymbol{u}|^2 dV$ is the fluid kinetic energy and dK/dt indicates the change rate of K over time. V is the integral volume, which refers to the domain of the flow channel. $\boldsymbol{\omega} = \nabla\times\boldsymbol{u}$ is the fluid vorticity. In the equation, the first line presents two expressions for the work of Lorentz force P_{LF}. The terms in the second line are the powers of the pressure energy term P_p, the turbulent convection term P_k, the vortex force term P_{VF}, and the enstrophy term P_{En}. This equation indicates that the energy input by the Lorentz force in the fluid is converted into the five terms, among which the fluid pressure energy is the desirable destination for the energy conversion in ALIP.

The simulation results were processed in the same way as the treatment for the equation of the magnetic energy. The time histories of the various terms in Equation 11 are illustrated in Figure 15 over a period time of $t = 0.8 \sim 1.8$ s. It is seen that the work of Lorentz force and the fluid pressure energy are the major parts of the equation. The work of vortex force is also significant, while the other fluid-related terms are marginal and will be ignored in the discussion. By viewing the average values of P_{LF} and P_P, approximately 80% of the work of Lorentz force is converted into the fluid pressure energy in the ALIP. Most of the rest energy is converted into the work of vortex force. Like the behavior of P_{LF}, the fluid pressure energy is also strongly fluctuated with time. This fluctuation directly corresponds to the pressure pulsation of low frequency, since the pressure pulsation of DSF has been eliminated by the time-averaged data processing method. It is seen that the fluctuations of P_p and P_{VF} are gradually reduced when the surface current density is changed from J_{s1} to J_{s3}. This result indicates that the addition of the modulated surface current density has improved the stability of the flow and the processes of energy conversion in the ALIP. It is also found that the ratio of the energy conversion from P_{LF} to P_p remains nearly constant when the modulated surface current density is imposed. Therefore, the efficiency of energy conversion is marginally influenced by the active flow control method.

3.5. Analysis on Energy Efficiency of the Active Flow Control Method. The quantitative analysis on the energy efficiency of the active flow control method will be presented in this section. One difficulty for estimating the total energy efficiency lies in the missing of the total input energy from the external

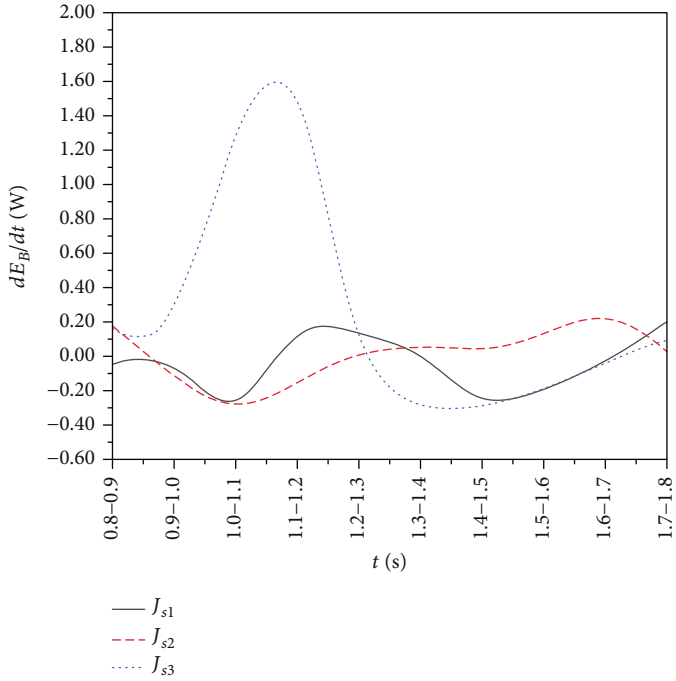

(a) Temporal change rate of magnetic energy dE_B/dt

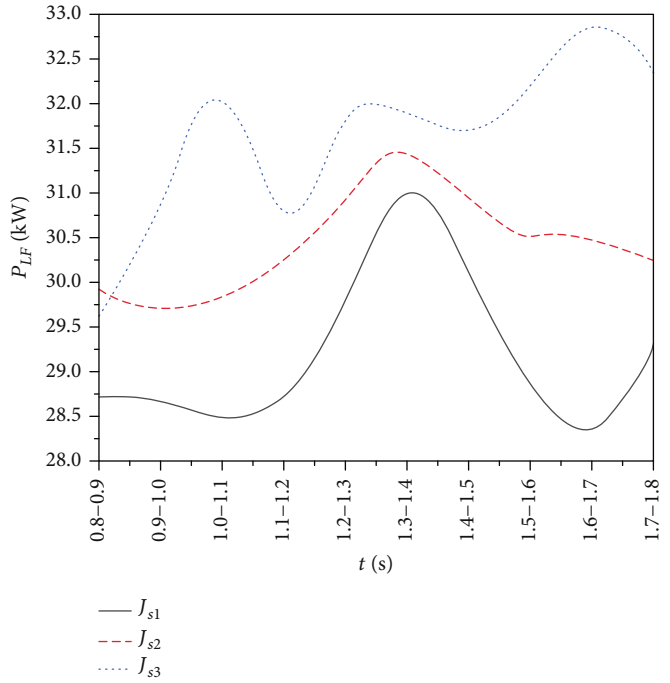

(b) Work of Lorentz force P_{LF}

Figure 14: Continued.

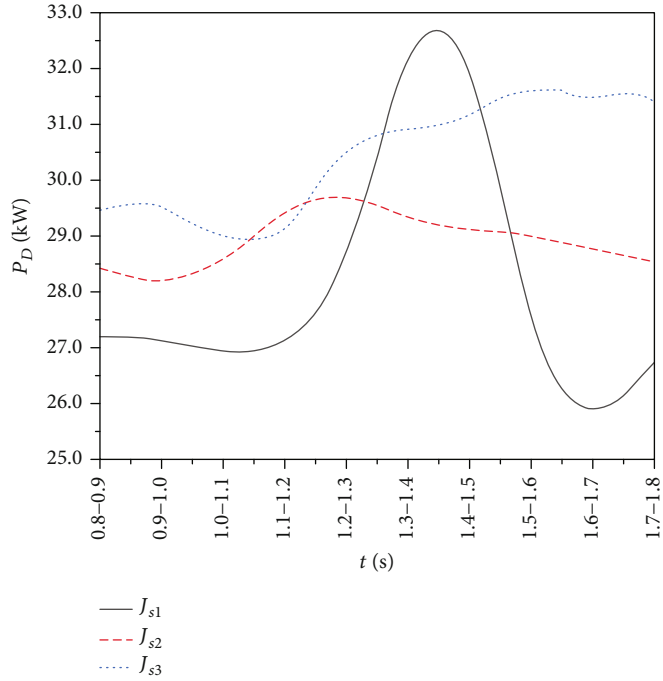

(c) Ohmic dissipation P_D

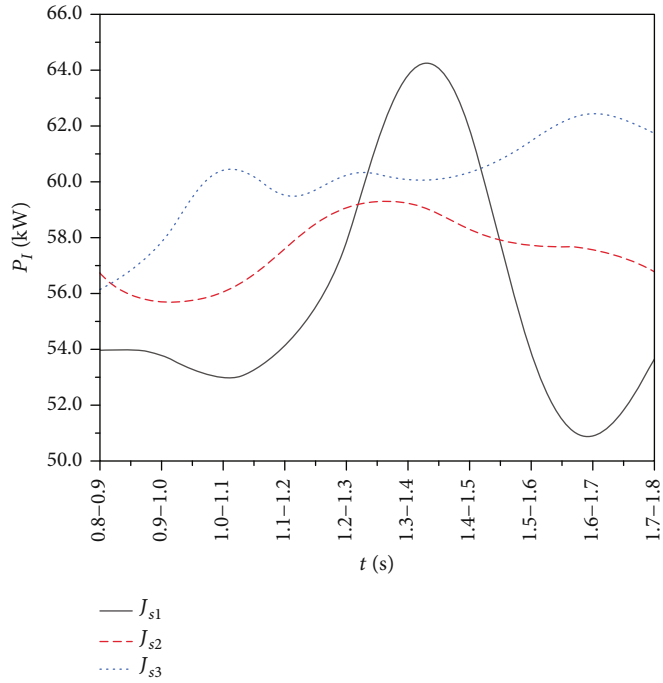

(d) Input energy P_I

Figure 14: Time histories of various mechanisms of energy conversion between magnetic field and fluid.

power source. In the simplified model, P_I only calculates the input energy of the stimulated magnetic field from the boundary of the flow channel. It is noticed in Equations (9) and (10) that the modulated surface current density J_{sm} is of the same form as the background surface current density J_s. It can be assumed that both methods are equally efficient in converting the energy from the external power source to the surface current density. The total input energy from the power source to the ALIP is defined as P_{Ie}. For the modulated surface current density J_{s2}, the strength factor β of the modulated part is 0.1, and it is only applied in half of the perimeter of the flow channel ($0.5\pi < \varphi < 1.5\pi$). The energy required for the modulated surface current density is approximately 0.05 times the input energy required for

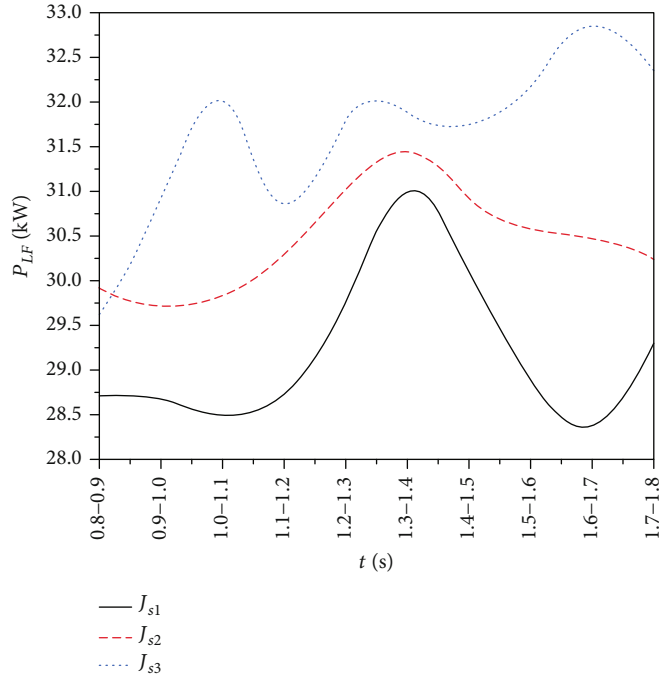

(a) Power of Lorentz force P_{LF}

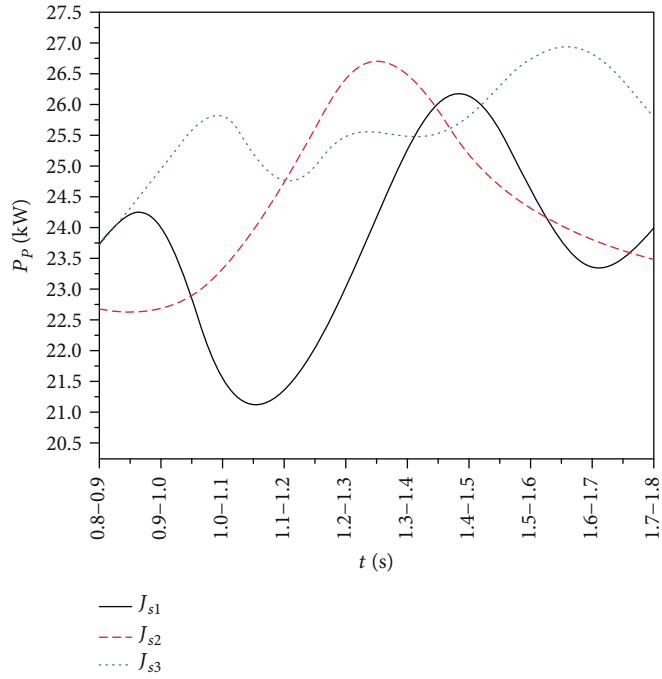

(b) Power of pressure P_p

Figure 15: Continued.

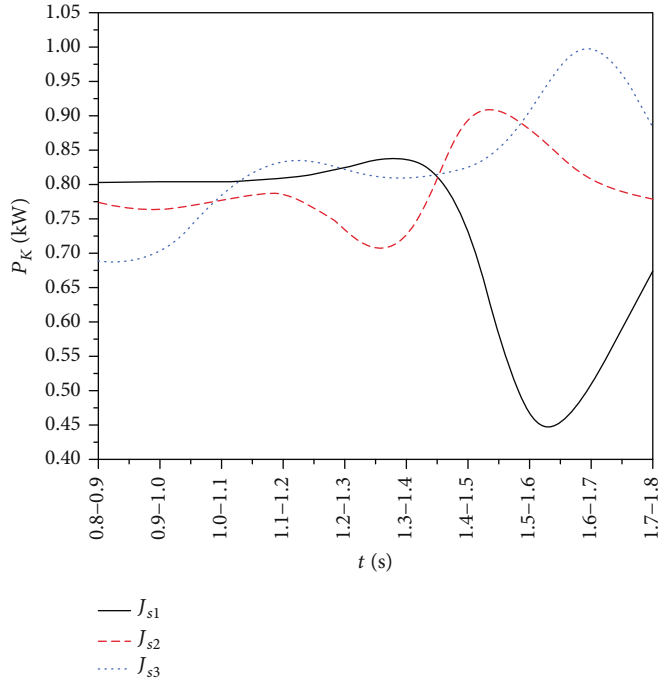

(c) Turbulent convection P_K

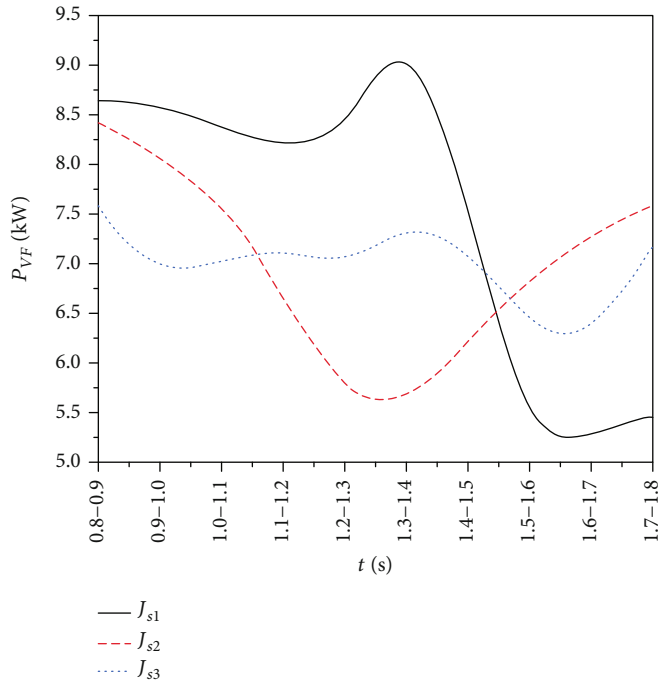

(d) Work of vortex force P_{VF}

Figure 15: Continued.

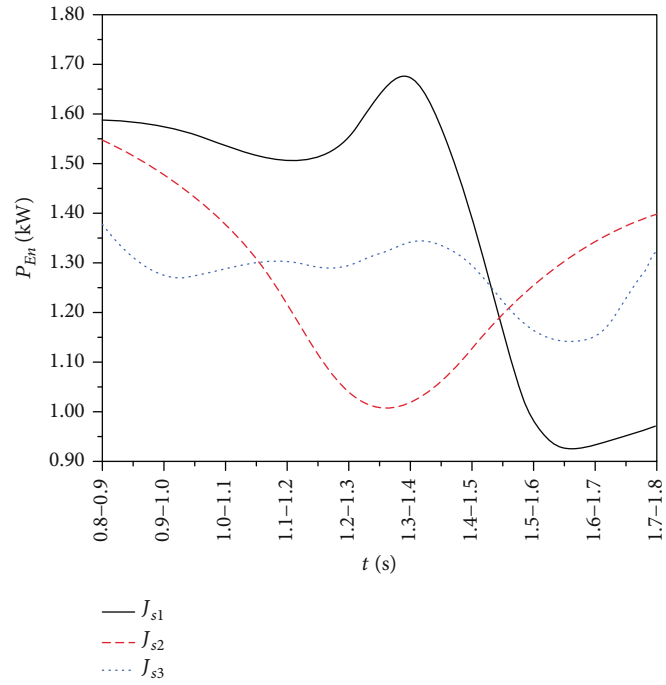

(e) Work of enstrophy P_{En}

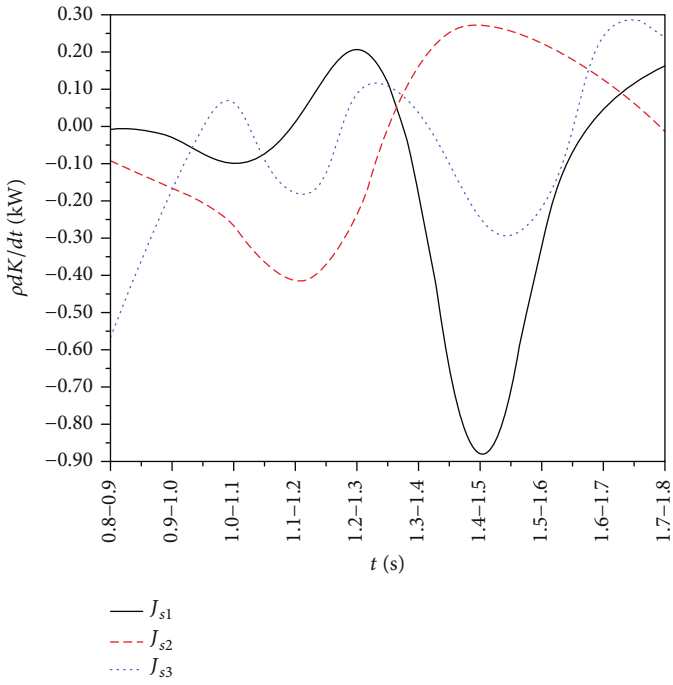

(f) $\rho dK/dt$

Figure 15: Time histories of various mechanisms of energy conversion in the fluid.

the background surface current density. Therefore, the total input power P_{Ie} at J_{s2} and J_{s3} is 1.05 times and 1.15 times that at J_{s1}, respectively. The total input power $P_{Ie} = 85270$ W at J_{s1} condition can be found in the reference data [9], and thus, the total input powers at J_{s2} and J_{s3} are approximately calculated as 89533.5 W and 98060.5 W, respectively. The fluid pressure energy P_p, the input energy from the surface current density P_I, and the total input energy from the power source P_{Ie} are illustrated in Figure 16(a) under three different surface current densities. The conversion efficiencies from the external power source to the fluid pressure are also calculated and compared in Figure 16(b).

The results show that both the fluid pressure energy and the input energy increase as the modulated surface current

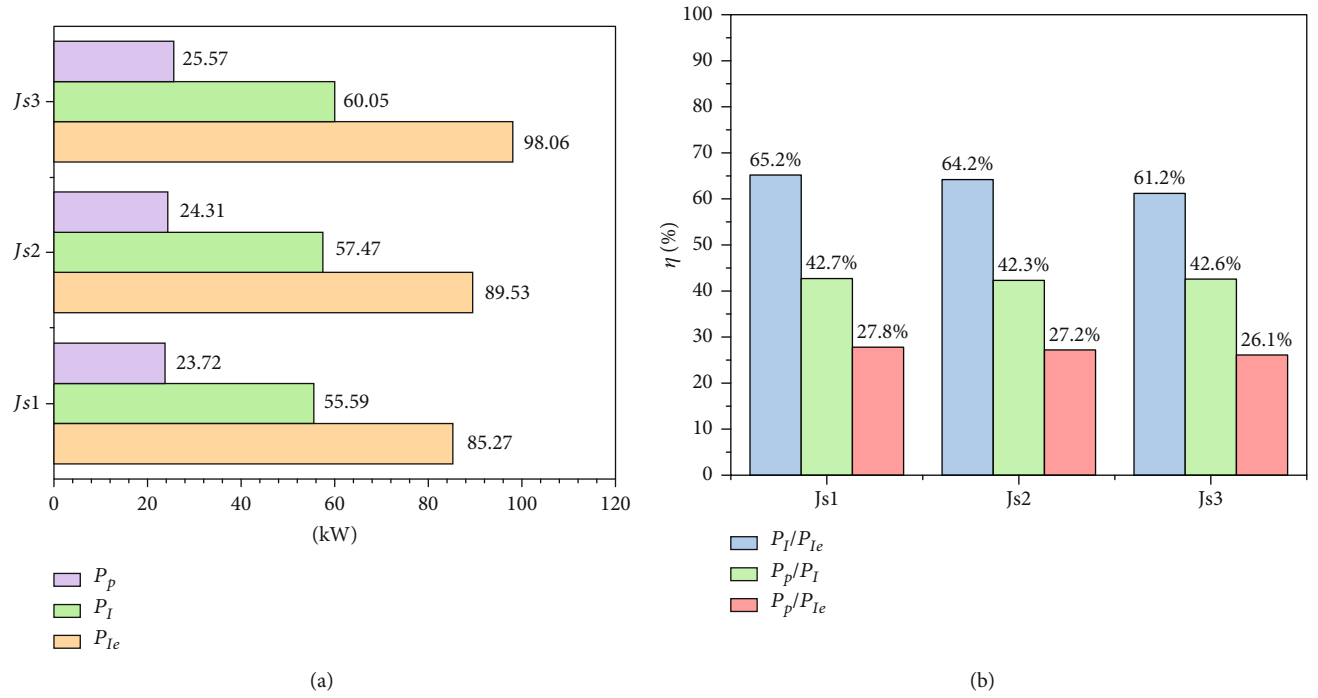

Figure 16: Efficiency of energy conversion at different modulated surface current densities.

density is intensified from J_{s1} to J_{s3}. Whether it is obtained from the simulation result or the empirical calculation, the increases of P_I and P_{Ie} are very limited. It is also seen that approximately 61%~65% of P_{Ie} is converted into P_I while approximately 42% of P_I is converted into P_p. The overall efficiency of energy conversion of the ALIP is estimated at 27.8% at J_{s1} condition. If the modulated surface current density is activated, this parameter is reduced to 27.2% and 26.1% at the J_{s2} and J_{s3} working conditions, respectively. Even at the lowest efficiency, an overall decrease of 1.7% is acceptable at J_{s3} condition where the flow stability and the pressure pulsation are significantly improved. The analysis on the energy efficiency proves that the proposed flow control method is also desirable from the perspective of energy efficiency.

4. Conclusion

In this work, a 3D numerical model considering the coupling between the fluid and magnetic field in ALIP is employed, and the full-scale pump channel is simulated in order to accurately capture the unstable flows evolved in the ALIP. An active flow control strategy is applied to suppress the unstable flows under the off-design conditions. The validation and energy efficiency of the active flow control method are estimated based on the simulation results.

The results have shown that the modified surface current accelerates the evolution of the large-scale vortices in the flow channel. It also suppresses the size and strength of the vortices, promoting the flow stability in the ALIP. The pressure pulsation of low frequency at the ALIP's outlet is significantly reduced if the strength of the modulated surface current density reaches a certain level. The processes of energy conversion in the ALIP are also improved more stable by the active flow control method. It is found that the fluctuations in various mechanisms of energy conversion are attenuated as the strength of the modulated surface current density increases. Finally, it is found that the overall energy efficiency is slightly reduced even when the modulated surface current density reaches the maximum level in this work. These improvements will increase the stability and reliability of the ALIP device. Before this work, there are two published controlling methods: winding grating at both ends of ALIP and installation of guide vanes. Both methods will cause significant loss in energy efficiency. This method causes less reduction in the energy efficiency compared with the previous controlling methods. However, this work only demonstrates a conception of active flow control in the unstable flows of the ALIP. More efforts should be done to realize the engineering implementation of this method.

Data Availability

The data that support the findings of this study are available from the corresponding author upon reasonable request.

Conflicts of Interest

The authors declare that there is no conflict of interest regarding the publication of this paper.

Authors' Contributions

The persons who made significant contributions in this work are all listed as the coauthors. All authors have read and agreed to the published version of the manuscript.

Acknowledgments

The authors are grateful for the financial support from the National Natural Science Foundation of China (Grant No. 52176038) and Key R & D Projects in Jiangsu Province (Grant No. BE2021073).

References

[1] O. M. Al-Habahbeh, M. Al-Saqqa, M. Safi, and T. A. Khater, "Review of magnetohydrodynamic pump applications," *Alexandria Engineering Journal*, vol. 55, no. 2, pp. 1347–1358, 2016.

[2] L. R. Blake, "Conduction and induction pumps for liquid metals," *Proceedings of the IEE Part A: Power Engineering*, vol. 104, no. 13, pp. 49–67, 1957.

[3] J. F. Mondt, V. C. Truscello, A. T. Marriott, M. S. El-Genk, and M. D. Hoover, "SP-100 power program," *AIP Conference Proceedings*, vol. 301, no. 1, pp. 143–155, 1994.

[4] F. Zhang, K. A. Adu-Poku, B. Hu, D. Appiah, and K. Chen, "Flow theory in the side chambers of the radial pumps: a review," *Physics of Fluids*, vol. 32, no. 4, article 041301, 2020.

[5] A. Andreev, V. G. Danilin, B. G. Karasev, and I. R. Kirillov, "Choice of construction schemes of electromagnetic pumps for atomic energy stations with fast reactors," *Magnitnaya Gidrodinamika*, vol. 18, no. 1, 1982https://www.osti.gov/biblio/5871228.

[6] H. Araseki, I. R. Kirillov, G. V. Preslitsky, and A. P. Ogorodnikov, "Magnetohydrodynamic instability in annular linear induction pump," *Nuclear Engineering and Design*, vol. 227, no. 1, pp. 29–50, 2004.

[7] G. Srinivasan, K. V. S. Kumar, B. Rajendran, and P. V. Ramalingam, "The fast breeder test reactor—design and operating experiences," *Nuclear Engineering and Design*, vol. 236, no. 7-8, pp. 796–811, 2006.

[8] A. M. Anisimov, I. V. Vitkovsky, M. M. Golovanov et al., "Electromagnetic pumps for BN-800," *Atomic Energy*, vol. 112, no. 6, pp. 443–446, 2012.

[9] R. Zhao, X. Dou, J. Huang, D. Zhang, D. Xia, and X. Zhang, "Mechanisms of energy conversion in induction magnetohydrodynamic pumps for transporting conducting liquids," *Energy*, vol. 244, article 123157, 2022.

[10] A. Fanning, G. Kliman, W. Kwant et al., "Giant electromagnetic pump for sodium cooled reactor applications," in *IEEE International Electric Machines and Drives Conference, 2003. IEMDC'03*, vol. 1, pp. 477–482, Madison, WI, USA, June 2003.

[11] A. Gailitis and O. Lielausis, "Instability of homogeneous velocity distribution in an induction-type MHD machine," *Magnitnaya Gidrodinamika*, vol. 1, pp. 87–101, 1975.

[12] I. R. Kirillov and V. P. Ostapenko, "Local characteristics of a cylindrical induction pump for Rm s > 1," *Magnetohydrodynamics*, vol. 23, no. 2, 1987https://www.osti.gov/biblio/7012484.

[13] H. Araseki, I. R. Kirillov, G. V. Preslitsky, and A. P. Ogorodnikov, "Double-supply-frequency pressure pulsation in annular linear induction pump: Part I: Measurement and numerical analysis," *Nuclear Engineering and Design.*, vol. 195, no. 1, pp. 85–100, 2000.

[14] F. Werkoff, "Finite-length effects and stability of electromagnetic pumps," *Experimental Thermal and Fluid Science*, vol. 4, no. 2, pp. 166–170, 1991.

[15] H. R. Kim and Y. B. Lee, "MHD stability analysis of a liquid sodium flow at the annular gap of an EM pump," *Annals of Nuclear Energy*, vol. 43, pp. 8–12, 2012.

[16] Z. Ruijie, D. Xiaohui, P. Qiang, Z. Desheng, and B. P. M. van Esch, "Analysis on the inception of the magnetohydrodynamic flow instability in the annular linear induction pump channel," *Journal of Fluids Engineering*, vol. 143, no. 6, article 061208, 2021.

[17] P. Blanc, T. Xuan, and R. Deshais, "Design calculations for annular induction electromagnetic pumps based on the finite element method," *IEEE Transactions on Magnetics*, vol. 4, no. 2, pp. 166–170, 1982.

[18] C. Gissinger, P. R. Imazio, and S. Fauve, "Instability in electromagnetically driven flows. I," *Physics of Fluids*, vol. 28, no. 3, article 034101, 2016.

[19] P. R. Imazio and C. Gissinger, "Instability in electromagnetically driven flows. II," *Physics of Fluids*, vol. 28, no. 3, article 034102, 2016.

[20] T. Asada, R. Aizawa, T. Suzuki, Y. Fujishima, and E. Hoashi, "3D MHD simulation of pressure drop and fluctuation in electromagnetic pump flow," *Mechanical Engineering Journal*, vol. 2, no. 5, 2015.

[21] T. Asada, Y. Hirata, R. Aizawa, Y. Fujishima, T. Suzuki, and E. Hoashi, "Development of a three-dimensional magnetohydrodynamics code for electromagnetic pumps," *Journal of Nuclear Science and Technology*, vol. 52, no. 5, pp. 633–640, 2015.

[22] K. I. Abdullina, S. V. Bogovalov, and Y. P. Zaikov, "3D numerical modeling of liquid metal turbulent flow in an annular linear induction pump," *Annals of Nuclear Energy*, vol. 111, pp. 118–126, 2018.

[23] R. Zhao, H. Li, D. Zhang, J. Huang, and W. Shi, "Numerical investigation of pump performance and internal characteristics in ALIP with different winding schemes," *International Journal of Applied Electromagnetics and Mechanics*, vol. 57, no. 1, pp. 39–51, 2018.

[24] R. Zhao, X. Dou, D. Zhang, and J. Huang, "Numerical study of the magnetohydrodynamic flow instability and its effect on energy conversion in the annular linear induction pump," *Physics of Fluids*, vol. 33, no. 6, article 067125, 2021.

[25] H. Araseki, I. R. Kirillov, G. V. Preslitsky, and A. P. Ogorodnikov, "Double-supply-frequency pressure pulsation in annular linear induction pump, part II: reduction of pulsation by linear winding grading at both stator ends," *Nuclear Engineering and Design*, vol. 200, no. 3, pp. 397–406, 2000.

[26] H. Araseki, I. R. Kirillov, G. V. Preslitsky, and A. P. Ogorodnikov, "Magnetohydrodynamic instability in annular linear induction pump," *Nuclear Engineering and Design*, vol. 236, no. 9, pp. 965–974, 2006.

[27] S. Changdar and S. De, "Analytical investigation of nanoparticle as a drug carrier suspended in a MHD blood flowing through an irregular shape stenosed artery," *Iranian Journal of Science and Technology, Transactions A: Science*, vol. 43, pp. 1259–1272, 2019.

[28] A. Chatterjee, S. Changdar, and S. De, "Study of nanoparticle as a drug carrier through stenosed arteries using Bernstein polynomials," *International Journal for Computational Methods in Engineering Science and Mechanics*, vol. 21, no. 5, pp. 243–251, 2020.

[29] B. Bhaumik, S. Changdar, and S. De, "Combined impact of Brownian motion and thermophoresis on nanoparticle

distribution in peristaltic nanofluid flow in an asymmetric channel," *International Journal of Ambient Energy*, vol. 43, no. 1, pp. 5064–5075, 2022.

[30] S. Dolui, B. Bhaumik, and S. De, "Combined effect of induced magnetic field and thermal radiation on ternary hybrid nanofluid flow through an inclined catheterized artery with multiple stenosis," *Chemical Physics Letters*, vol. 811, article 140209, 2023.

[31] S. Dolui, B. Bhaumik, S. De, and S. Changdar, "Effect of a variable magnetic field on peristaltic slip flow of blood-based hybrid nanofluid through a nonuniform annular channel," *Journal of Mechanics in Medicine and Biology*, vol. 23, no. 1, article 2250070, 2023.

[32] S. Dolui, B. Bhaumik, S. De, and S. Changdar, "Biomedical simulations of hybrid nano fluid flow through a balloon catheterized stenotic artery with the effects of an inclined magnetic field and variable thermal conductivity," *Chemical Physics Letters*, vol. 829, article 140756, 2023.

[33] C. B. da Silva and J. C. F. Pereira, "Invariants of the velocity-gradient, rate-of-strain, and rate-of-rotation tensors across the turbulent/nonturbulent interface in jets," *Physics of Fluids*, vol. 20, no. 5, article 055101, 2008.

[34] M. S. Chong, A. E. Perry, and B. J. Cantwell, "A general classification of three-dimensional flow fields," *Physics of Fluids*, vol. 2, no. 5, pp. 765–777, 1990.

[35] B. J. Cantwell, "On the behavior of velocity gradient tensor invariants in direct numerical simulations of turbulence," *Physics of Fluids A: Fluid Dynamics*, vol. 5, no. 8, pp. 2008–2013, 1993.

[36] J. Soria, R. Sondergaard, B. J. Cantwell, M. S. Chong, and A. E. Perry, "A study of the fine-scale motions of incompressible time-developing mixing layers," *Physics of Fluids*, vol. 6, no. 2, pp. 871–884, 1994.